StageIV-IRC: A High-resolution Dataset of Extreme Orographic Quantitative Precipitation Estimates (QPE) Constrained to Water Budget Closure for Historical Floods in the Appalachian Mountains

Mochi Liao[1] and Ana P. Barros[1]

1. Civil and Environmental Engineering, University of Illinois Urbana-Champaign, Urbana, IL

Corresponding Author:

Dr. Ana Barros

E-mail: barros@illinois.edu

Phone: +1 217-333-8038

Abstract

Quantitative Flood Estimation (QFE) in complex terrain remains a grand challenge in operational hydrology due to the lack of accurate high-resolution Quantitative Precipitation Estimates (QPE) for operational forecasting and for calibrating hydrologic models. Here, we present a high-resolution (i.e., 250m, 5-minute-hourly) QPE dataset for 215 extreme rainfall events occurred in 26 gauged mountainous basins in the Appalachian Mountains from 2008 to 2024. This dataset is developed by applying inverse rainfall corrections (IRC) derived from physically-based rainfall-runoff modeling (Liao and Barros, 2022 and 2023) to the Next Generation Weather Radar (NEXRAD) Stage IV analysis (4 km resolution, hourly). The corrected Stage IV analysis QPE is referred to as StageIV-IRC (StageIV with Inverse Rainfall Correction). The unique advantage of this StageIV-IRC QPE dataset is its agreement with ground-based rainfall measurements while achieving water budget closure at the storm-flood event scale and minimizing uncertainty from initial conditions using the Initial Condition Correction (ICC) module. This dataset is the first QPE dataset aiming to improve QFE in the complex terrain by reducing biases for extreme precipitation events, and it can be used to evaluate the skill of hydrologic models in the same basins and support model calibration. The StageIV-IRC QPE dataset is publicly available at https://doi.org/10.5281/zenodo.14028866, and improved initial soil moisture maps for the studied extreme precipitation events, derived from the ICC module in the same IRC framework, are available in the same repository (Liao and Barros, 2025c).

1. Introduction

Over the past few decades, extreme precipitation has become an increasingly important research topic due to its social, economic, and environmental impacts (e.g., Alimonti et al., 2022; Wernberg et al., 2013). Studies show that both total annual precipitation and extreme precipitation events have increased in the US and in other parts of the world during the last century (e.g., Milly et al., 2002), often resulting in floods (e.g., Pielke and Downtown, 2002), and flash floods in the context of complex terrain due to steep slopes (e.g., Schumacher, 2017; Czigány et al., 2010). Flash floods are characterized by fast rainfall-runoff responses on the scale of a few hours (< 6 hours) after extreme precipitation events for watershed areas often ranging from a few tens to hundreds of square kilometers (e.g., Borga et al., 2014; Lumbroso and Gaume, 2012). As one of the deadliest natural hazards, flash floods are often associated with landslide events (e.g., Tao and Barros, 2014; Gupta et al., 2016; Deijns et al., 2022) and cause loss of life and property damage (Špitalar et al., 2014), such as recently in the last three years in the Appalachian Mountains, USA, and in Southern Spain. Despite extensive studies to improve flash flood simulations in small headwater basins, hydrological skill scores (e.g., Kling-Gupta Efficiency or KGE) remain poor at event scales largely due to significant difficulties involved in estimating highly localized orographic precipitation in complex terrain, which in turn implies that hydrologic models are not calibrated using forcing representative of realistic extreme events (e.g., Andrieu et al. 1997; Huffman et al., 2007; Mtibaa and Asano, 2022).

Current approaches involved in precipitation measurement and Quantitative Precipitation Estimation (i.e., QPE) broadly include in-situ point-scale observations using rain gauges and disdrometers, and remote spatial observations using ground-based radar and space-based sensors. In complex terrain, there is often a scarcity of in situ measurements due to difficult access. For example, the rain gauge network from NASA's Integrated Precipitation and Hydrology Experiment is the only relatively dense rain gauge network installed at high elevations in the entire Appalachians (e.g., Barros et al. 2014). Other QPE products (e.g., radar QPE data) are plagued by uncertainties from various sources (e.g., ground clutter artifacts, retrieval uncertainties, and radar viewing geometry (Villarini and Krajewski, 2010; Arulraj and Barros, 2021; Kreklow et al., 2020; Huffman et al., 2007; Andrieu et al., 1997; Durden et al., 1998). Numerical weather prediction (NWP) is an alternative to measurement. However, QPE products from NWP models are characterized by significant uncertainties when evaluated against rain gauges (e.g., Zhang and Anagnostou, 2019), leading to large flood simulation errors when used as inputs to hydrological models, or introducing large structural uncertainty when used for model calibration (e.g., Tao et al., 2016; Weiland et al., 2015; Diomede et al., 2008; Kobold and Suselj, 2005). Due to these uncertainties and errors involved, focus has been directed towards enhancing QPE using various methods: data merging of raingauge and radar precipitation (e.g., McKee and Binns, 2016; Goudenhoofdt and Delobbe, 2009; Delrieu et al., 2014; Nanding et al., 2015; Sideris et al. 2013; Schiemann et al. 2011), combined radar reflectivity and retrieval corrections (e.g., Vignal et al., 2000; Shao et al., 2021; Dinku et al., 2002), and data assimilation into NWP models (e.g., Rafieeinasab et al., 2015; Wehbe et al., 2020). Rain gauge and disdrometer measurements are often used as references for these QPE optimization approaches (e.g., Harrison et al., 2000; Shao et al., 2021; Fulton et al., 1998). The ‘ground truth’, however, has its own error (e.g., spatial representativeness, wind artifacts around the gauge orifice, and calibration, among others; Kochendorfer et al., 2017), and fails to capture highly localized orographic enhancement (e.g., Prat and Barros, 2010b; Gentilucci et al., 2021; Buytaert et al., 2006). Gauge-radar fusion often relies on geostatistical assumptions that are primarily distance-based (e.g., Areerachakul et al., 2022;

Cassiraga et al., 2021; Wang et al., 2020; Maggioni and Massari, 2018), lacking the full picture of complex basin topography, which has a regulating role in orographic precipitation processes.

To address this long-standing QPE challenge in complex terrain, a general QPE error quantification framework was developed leveraging widely available quality United States Geological Survey (USGS) streamflow observations at the outlet of headwater basins in complex terrain, consisting of 2 distinct paths: 1) rain gauge bias correction, and 2) grid-level QPE correction constrained to watershed-scale water budget closure. The first pathway includes rain gauge bias corrections at gauge locations both at the diurnal and climate scales, and the geostatistical distribution of rain gauge biases across a basin. The second pathway includes an innovative inverse QPE correction method by backward propagating runoff uncertainty using a hydrological model via streamlines to precipitation at storm-event scale, and the methodology is termed Inverse Rainfall Correction (IRC), which is developed by the same authors (Liao and Barros, 2022 or LB22). The IRC was initially developed in the Southern Appalachians and later extended to headwater basins over a span of 2,000 km from south to north along the entire Appalachian Mountains. It is worth noting that rain gauges are only available in the Southern Appalachians, thus elsewhere the StageIV product was downscaled to 250m first and then submitted to the IRC without bias corrections or any other intermediate corrections as in LB22. The generalizability of the IRC framework, regardless of rain gauge bias corrections beforehand, is demonstrated in Liao and Barros (2023).

LB22 found that initial soil moisture uncertainty causes inferior performance of IRC because large initial condition errors lead to significant uncertainties in travel time distributions. Soil moisture is considered a particularly important factor among soil properties due to its significant role in affecting the generation of runoff, hence dramatically altering the timing of flood front and its magnitudes (e.g., Vivoni et al., 2007; Marchi et al., 2010; Penna et al., 2011), and soil moisture can vary dramatically at hourly timescales, changing from fully saturation levels to wilting point levels conditional on the specific texture and other properties of the soils (Grillakis et al., 2016). Initial soil moisture conditions can therefore determine whether a rainstorm produces a major flash flood or not (e.g., Komma et al., 2007; Zehe and Blöschl, 2004). However, due to the limited availability of soil moisture sensors, there are not many studies quantifying the impact of soil moisture on runoff simulation (e.g., Silvestro et al., 2019; Laiolo et al., 2016; Zappa et al., 2011; Uber et al., 2018). Liao and Barros (2025b) developed an Initial Condition Correction (ICC), which is based on travel time distributions and is coupled with the general IRC approach, demonstrating large improvements in initial soil moisture estimation. Note that when implementing the IRC and ICC, we are using a fully distributed physics-based uncalibrated model (i.e. Duke Coupled Hydrological Model, DCHM) that has been used successfully for more than two decades for hydrologic studies in the Southern and Central Appalachians (e.g., Tao and Barros, 2013, 2014, 2018 and 2019; Tao et al. 2016; Yildiz and Barros 2004, 2007 and 2009), and consequently uncertainty from model structure and model parameters is assumed to be small. Hydrological model parameters certainly have an impact on rainfall-runoff response, but they are generally only of secondary importance compared to the precipitation proper and antecedent soil moisture distributions, especially for smaller basins (e.g., Dobler et al., 2012; Mockler et al., 2016).

In this work, IRC and ICC are combined into one framework , referred to as the IRC-ICC framework in Liao and Barros (2025b), to construct an improved QPE dataset aiming to close the water budget at the scale of storm-flood events along the entire Appalachian Mountains range, The study region is set to be the Appalachian Mountains because they are prone to extreme precipitation and flash floods due to orographic lift of moisture-laden air masses coming from the

Gulf of Mexico and the Atlantic Ocean (e.g., Troch et al., 1994; Smith et al., 2011; Liao and Barros, 2023). A recent example is Hurricane Helene, which caused over 200 deaths and over $50 billion in property damage in the Southeast US in September 2024. The IRC-ICC framework is employed in 26 headwater basins and 215 extreme events (during 2008-2024) using the Next Generation Weather Radar (NEXRAD) StageIV dataset as original inputs, at a spatial and temporal resolution of 250 m and 5 minutes, respectively, and the improved post IRC-ICC QPE data (i.e., StageIV-IRC) are made available in this study.

The manuscript is organized as follows. The data sources and the QPE error quantification framework, which consists of rain gauge bias correction and the IRC-ICC framework, are detailed in Section 2. Section 3 presents this new dataset (StageIV-IRC) along with data assessment from various aspects. Section 4 discusses the potential application of this new dataset and future work. Section 5 provides access to the dataset and a summary of the work.

2. Data and Methodology

2.1 Radar QPE StageIV

The NCEP/EMC StageIV is a precipitation estimation product, developed using hourly and 6-hourly radar-raingauge precipitation analyses at regional scales (Lin and Mitchell, 2005). In complex terrain, it is known that radar QPE suffers from the blockage of topography, overshooting and retrieval uncertainties, leading to large uncertainties in rainfall estimation. In 2007, as part of the ground validation (GV) of the Precipitation Measurement Missions (PMM) program by NASA (e.g., Prat and Barros, 2010a and 2010b), 34 tipping bucket raingauges were installed in the Southern Appalachians and have been well-maintained since 2007 (e.g., Barros et al., 2014). In this work, raingauge measurements from a GV raingauge network are utilized to reduce StageIV uncertainties in the Southern Appalachians.

2.2 GV Rain Gauge Observations

A rain gauge network in support of PMM GV was installed in the Pigeon River basin for the 10 year 2007-2018 period (Barros et al. 2014). A map of this rain gauge network is plotted in Figure 1. Every rain gauge is labelled with a number, and exact locations are documented in Table 1. This rain gauge network is regularly visited and maintained at least three times a year, including on-site cleaning and calibration. In this study, these rainfall measurements are used as a basis to adjust hourly StageIV QPE. Note these rain gauge measurements can be downloaded at http://dx.doi.org/10.5067/GPMGV/IPHEX/GAUGES/DATA301 (Barros et al., 2017). Besides rain gauges, a network of Parsivel disdrometers was installed during 2013-2014, with each disdrometer location denoted by the letter P in Figure 1. These disdrometer data were only used for independent evaluation because of short records. It is worth noting that rain gauges are installed mostly along the ridges while disdrometers are generally located at lower elevations.

<Figure 1 here please>

2.3 Methodology

The methodology of this work includes four major elements: a) rain gauge bias and climatology corrections where raingauge data are available, b) downscaling of radar precipitation,

c) grid-scale QPE correction by closing the water budget using stream gauge measurements, and d) basin and event selection procedures and model setup.

2.3.1 Rain Gauge Corrections

A schematic drawing of the rain gauge correction framework to derive gauge-improved QPE (named StageIV$_{DBKC}$) is provided in Figure 2. The subscripts DBKC refer to '**D**ownscaled', '**B**ias correction using rain gauge measurements at gauge locations', '**K**riging interpolation in 2D', and '**C**limatological corrections', respectively.

<Figure 2 here please>

First, to make meaningful comparison between StageIV estimates and rain gauge measurements spatially, a fractal downscaling algorithm is used to create StageIV$_D$ at 1km from the original StageIV at 4km resolution. Subsequently, bias correction using raingauge measurements is employed to create StageIV$_{DB}$ at hourly timescales. StageIV$_{DB}$ data are then evaluated against the rain gauge climatology from 2008 to 2017 to reduce biases that depend on weather regime, and climatological biases are then spatially interpolated using the ordinary Kriging method. The resulting dataset is named StageIV$_{DBKC}$ (abbreviated as STIV$_{DBKC}$).

2.3.2 Fractal downscaling

The methodology for fractal downscaling was first proposed by Bindlish and Barros (1996) and subsequently demonstrated through various applications to precipitation downscaling from models (Bindlish and Barros, 2000) and remote sensing data (Nogueira and Barros, 2015; Tao and Barros, 2010). Here, a brief description is presented.

The assumption of self-similarity is imposed in fractal downscaling approach. The parameters used in this approach involve: fractal dimension *D*, Hurst coefficient *H*, and the spectral exponent β that are related through the following equations:

$$D = \frac{7-\beta}{2} \tag{1}$$

$$H = \frac{\beta-1}{2} \tag{2}$$

The parameter β describes rainfall statistics across different spatial scales, and it is calculated as the slope of the power spectral density curve in the 2D Fourier domain of the rainfall field (log-log plot). The parameter H is the Hurst coefficient which is a measure of autocorrelation strength with higher value representing stronger autocorrelation. The 2D Fourier transform of a rainfall field $z(x,y)$ is calculated as the following:

$$Z(u,v) = \left(\frac{L}{N}\right)^2 \sum_{x=0}^{N-1} \sum_{y=0}^{N-1} z(x,y)\, exp\left[-\frac{2\pi i}{N}(ux+vy)\right] \tag{3}$$

where N is the total number of grid points of the rainfall field z(x,y) with grid size being the L, u and v correspond to frequency indices in the Fourier domain in each direction. Using Eq. 3, the averaged power spectral density is given:

$$S_j = \frac{1}{L^2 N_j} \sum_1^{N_j} |Z(u,v)|^2 \tag{4}$$

where N_j denotes the number of points that meet the following condition: $j < \sqrt{u^2+v^2} < j+1$. The mean power spectral density and the wavenumber *k* (Eq.5) are related by a power law (Eq. 6):

$$k = \frac{2\pi}{\sqrt{u^2+v^2}} \tag{5}$$

$$S \sim k^{-\beta-1} \tag{6}$$

By applying a logarithmic transformation, the power-law relation between S and k is linearized, and the S value when wavenumber k = 1 is the roughness factor, which is a representation of the variance of the field.

Assuming rainfall fields have self-similar statistics expressed by a power-law, then fine scale rainfall fields can be generated from the coarse scale radar observations by preserving these self-similar statistics. This is accomplished by creating a Brownian surface at desired fine scale resolution while sharing the same spectral slope and roughness factor as the original rainfall field based on Bindlish and Barros (1996):

$$Z_D(u,v) = \frac{Z_b(u,v)}{k_r^{(\beta-\beta_b)/2}} exp\left[\frac{1}{2}\left(S_{r,1} - \frac{\beta+1}{\beta_b+1} S_{r,2}\right)\right] \tag{7}$$

where β, β_b, $Z_D(u,v)$ and $Z_b(u,v)$ are the spectral slope of 2D original rainfall field, the spectral slope of the Brownian surface, interpolation surface in the Fourier domain and original Brownian surface, respectively; k_r is the wavenumber and $S_{r,1}$ and $S_{r,2}$ are the roughness factors of the 2D original rainfall fields and Brownian surface. Due to the non-uniqueness of Brownian surfaces, multiple replicates of interpolation surfaces Z_D must be generated. In this study, an ensemble of ND (Number of Downscaled samples) interpolation surfaces is derived from the original StageIV product where ND=50 following Nogueira and Barros (2015), and thus fifty rainfall field realizations at finer resolution preserving the same rainfall statistics at coarse resolution is generated, and the ensemble mean was calculated. Finally, the rainfall correction steps described in Figure 2 are applied to the ensemble mean of the downscaled rainfall fields.

2.3.3 Climatology Corrections

The *__first__* phase of bias correction is carried out at the event scale: a linear regression is established between rain gauge measurements and collocated downscaled radar pixel estimates using the following formula:

$$R_g^t(i_g, j_g) = \kappa R_r^t(i_g, j_g) + \varepsilon \tag{8}$$

where R_r and Rg represent radar and rain gauge measurements respectively, κ and ε are the slope and the intercept of a polynomial fit between R_r and Rg. Hourly $\mathrm{StageIV_D}$ estimates and corresponding rain gauge observations in the same $\mathrm{StageIV_D}$ pixel were identified if at least 2 rain gauges in the same $\mathrm{StageIV_D}$ pixel measure non-zero rainfall. A linear regression was applied to all $\mathrm{StageIV_D}$ pixels within one standard deviation of the regression line at an hourly timescale by assuming homogeneity of variances or homoscedasticity.

The *__second__* phase of bias correction is done at decadal scale: aiming to reduce systematic radar errors caused by retrieval uncertainties and viewing geometry in complex terrain, demonstrating strong diurnal (time of day) and seasonal (weather regime) error dependencies due to missed detection of shallow rainfall systems related to radar overshooting in the Southern Appalachian when comparing against 10-year rain gauge observations (e.g., Prat and Barros, 2010b; Wilson and Barros, 2014; Duan et al. 2015; and Barros, 2017). For this purpose, when rain gauge observations are < 2mm/hr and Stage $\mathrm{IV_D}$ estimates are 0 mm/hr, the $\mathrm{StageIV_D}$ value was automatically replaced by the rain gauge observations, which is referred to as the Light Rainfall Correction (LRC). Moreover, if $\mathrm{StageIV_D}$ rainfall intensity is zero where at least one collocated rain gauge observation is > 2mm/hr, then $\mathrm{StageIV_D}$ estimates are replaced by the mean of all collocated rain gauge observations, namely Mean Rainfall Correction (MRC). Lastly, for highly localized precipitation (i.e., fewer than 2 rainguages register nonzero rain in the study domain) which is normally associated with small-scale convective activity, the rainfall differences between the StageIV$_D$ and the local rain gauge observations were bilinearly distributed across nearby grids (a 5x5 grid square centered at the StageIV$_D$ pixel) – Convective Rainfall Correction (<u>CRC</u>). For most of the raining hours, there are more than 2 rain gauges with nonszero rainfall, in which case the differences between radar estimates and raingauge measurements were spatially interpolated using ordinary Kriging , which is refered to as the Global Rainfall Correction (<u>GRC</u>).

2.3.4 Ordinary Kriging

Ordinary Kriging is a geostatistical interpolation method that generates artificial values of a variable at a specific location, aiming to minimize spatial variance. In this work, rainfall differences between raingauge observations and StageIV$_{DB}$ are calculated and distributed across the entire basin using a spatial variance model, which is commonly referred to as a semi-variogram model. Specifically, a spherical semi-variogram model is used. Literature regarding the choice of semi-variogram models and their properties can be found (e.g., Li and Heap, 2008; Oliver and Webster, 2015; Zimmerman and Zimmerman, 1991). Bohling (2005) pointed out that spherical models reach the maximum variance for relatively shorter spatial lags, therefore more suitable to capture highly nonlinear and localized orographic precipitation (McBratney and Webster, 1986):

$$\gamma(h) = C_0 + (C - C_0)\left(\frac{3h}{2d} - \frac{1}{2}\left(\frac{h}{d}\right)^3\right) \quad \text{if} \quad 0 \le \mathrm{h} \le \mathrm{d} \qquad (9.1)$$

$$= C \qquad \text{if} \quad \mathrm{h} > \mathrm{d} \qquad (9.2)$$

$$\gamma_{0i} = \frac{1}{N_A}\sum_{k=1}^{N_A}\gamma_{ki} \qquad (9.3)$$

$$\gamma_{00} = \frac{1}{N_A}\sum_{k=1}^{N_A}\sum_{l=1}^{N_A}\gamma_{kl} \tag{9.4}$$

where h is the lag, d is the range, C and C_0 are the sill and nugget values of the semi-variogram model, N_A is the number of raingauges. The nugget is assumed to be zero if local variability and measurement error are neglected at the point scales (Diggle and Ribeiro, 2007). The interpolated rainfall difference at a location x_0 $Z_{ok}^{*}(x_0)$ is calculated using a weighted combination of all available differences at gauge locations $G(x_i)$ multiplied by Ordinary Kriging weights λ_i^{ok}:

$$Z_{ok}^{*}(x_0) = \sum_{i=1}^{n}\lambda_i^{ok}G(x_i) \tag{10.1}$$

$$\sum_{i=1}^{n}\lambda_i^{ok} = 1 \tag{10.2}$$

Optimal Kriging weights can be obtained by a series of linear equations using the Lagrange multiplier μ method:

$$\begin{pmatrix} \gamma_{11} & \cdots & \gamma_{n1} & 1 \\ \vdots & \ddots & \vdots & \vdots \\ \gamma_{1n} & \cdots & \gamma_{nn} & 1 \\ 1 & \cdots & 1 & 0 \end{pmatrix} \begin{pmatrix} \lambda_1^{\mathrm{OK}} \\ \vdots \\ \lambda_n^{OK} \\ \mu \end{pmatrix} = \begin{pmatrix} \gamma_{01} \\ \vdots \\ \gamma_{0n} \\ 1 \end{pmatrix} \tag{11}$$

In this work, Ordinary Kriging interpolates differences between radar data and raingauge observations to produce gauge-corrected $\mathrm{STIV_{DBKC}}$ dataset. An example sequence of rainfall fields to illustrate the step-wise corrections described in Sections 2.3.1-2.3.4 is shown in Figure A1.

2.3.5 Precipitation Assessment Metrics

Assessment metrics include the following: bias and root mean square error between radar estimation and raingauge measurement, false alarm rate, the probability of detection (PD), threat score (TS) and Heidlke skill score (HSS), following McBride and Ebert, 2000. An instance when both radar QPE and rain gauge observation exceed a specified rain rate threshold is a hit (H); when observation matches the criterion and radar QPE does not, it is classified as a miss (M); if the opposite happens, then it is a false alarm (FA). The calculation of these metrics relied on a collection of Hs, Ms, and FAs:

$$Bias = \frac{1}{N}\sum_{n=1}^{N}(O_n - R_n) \tag{12}$$

$$RMSE = \sqrt{\frac{1}{N}\sum_{n=1}^{N}(O_n - R_n)^2} \tag{13}$$

$$FR = \frac{FA}{H+FA}, 0 \leq FR \leq 1 \tag{14}$$

$$PD = \frac{H}{H+M}, 0 \leq PD \leq 1 \tag{15}$$

$$TS = \frac{H}{H+FA+M}, 0 \leq TS \leq 1 \tag{16}$$

$$HSS = 2 * \frac{Z*H-FA*M}{\big((H+FA)*(Z+FA)\big)+\big((M+H)*(M+Z)\big)}, -1 \leq HSS \leq 1 \tag{17}$$

where O is the rain gauge observation, R is the radar QPE, and N is the number of points. Z represent the number of zeros, meaning both raingauge and radar do not register a rainfall record above a predefined threshold. A threat score (TS) of 0.5 means over 50% of cases meet the criterion, and the higher the better. An HSS of 0 means a forecast has the same performance as a random guess.

2.3.6 Inverse Hydrologic Correction

At flash flood timescales in headwater basins, streamflow uncertainty and precipitation uncertainty are strongly connected in a nonlinear way through rainfall runoff processes. Liao and

Barros (2022) developed a Lagrangian-based framework named Inverse Rainfall Correction (IRC), allowing backpropagating streamflow uncertainty to precipitation inputs in space and time through an uncalibrated distributed hydrological model (i.e., DCHM), achieving water budget closure at the event scale in small headwater basins. As stated earlier, the uncertainties associated with parameters and the hydrological model DCHM are neglected since the model configurations have been used and improved over the past two decades for this region accounting for various soil, vegetation, and river processes (e.g., Tao and Barros, 2013, 2014, 2018 and 2019; Yildiz and Barros, 2005 and 2007; Lowman and Barros, 2016), and the IRC framework has been tested in multiple headwater basins extensively in this region with consistent success. The detailed description of the IRC is provided in Section 2.3.8 and Appendix A.

It is worth noting that IRC is a general framework to improve QPE at the watershed scale that can be incorporated into any distributed hydrological models. Liao and Barros (2025a, 2025b) investigated the impact of model structure uncertainty and initial condition uncertainty on IRC and then the downstream product the resulting IRC improved QPE. The results suggest with improved watershed physics at finer resolution (e.g., river bank storage, Liao and Barros, 2025a), river routing algorithms (e.g., XY routing, Liao and Barros, 2025a) and improved antecedent soil moisture distributions (Liao and Barros, 2025b), post-IRC QPE demonstrate realistic precipitation features at high resolution that are aligned with basin topography with ridges associated with higher precipitation than valleys in general, showing a significant improvement from the original StageIV dataset which is characterized by unnatural boxy precipitation patterns in complex terrain due to resolution issues and over or underestimation depending on topography and distance from the radar site.

As briefly mentioned before, LB22 reviewed various sources of uncertainty that can prevent post-IRC QPE from achieving water budget closure, among which initial condition uncertainty in soil moisture is a noteworthy source. Improved initial condition estimation results in significantly improved post-IRC precipitation features in complex terrain by better capturing transient travel time distributions (Liao and Barros, 2025b). They found that the uncertainty tied to initial conditions is more significant for less extreme events. Nevertheless, the initial condition correction method is coupled with the IRC framework, and the complete framework is named the IRC-ICC framework. The specifics regarding the IRC, ICC, and IRC-ICC are schematically drawn in Figure 3.

<Figure 3 here please>

Using the definitions of characteristic timings shown in panels c) and d), characteristic flow regime windows are identified. In principle, the number and the size of the windows depend on the complexity of the hydrograph. ICC is only applied to windows 2 and 5 in this example, which represents a segment of the hydrograph characterized by the differences between rising points in observations and simulations, and a segment characterized by slow recession, respectively. The assumption is that precipitation uncertainty regulates streamflow differences during peak flows (i.e. windows 3 and 4). W_{nm} represents the framework state after window m for iteration n. The resolution settings for the DCHM are: spatial resolution: 250m, and temporal resolution: 5 minutes.

2.3.7 Implementation of Lagrangian Tracking

A flood event is simulated by the DCHM at the basin outlet with grid-based time-varying velocity fields for different soil layers. When the precipitation starts (i.e. basin-averaged precipitation > 0.1mm/hr), new particles (passive tracers) are launched at the same frequency of model temporal resolution (5 minutes), but only at non-zero precipitation grids in all soil layers following the velocity fields calculated by the DCHM, and the tracking resolution is 10 seconds, amounting to a release of approximately 600,000 particles for basin with an area of 120km^2 over a 24-hour period. During the tracking phase, each particle is saved along with information regarding its source location (grid-point where it originates), time of release ti, and travel time tT (tT is defined as the difference between current time t and the time of release ti, i.e., tT = t – ti). Multiple particles from different source locations can have the same travel time, which is the basis for identifying the number of trajectories contributing to the hydrograph at the outlet as a function of time.

2.3.8 QPE Correction Using IRC

At time t, the water difference *wd(t)* between the observed and simulated streamflow over the time *Δt* between two consecutive discharge observations represents the fraction of runoff that eventually leaves the basin as streamflow. Errors in precipitation forcing propagate to the runoff, under the assumption of negligible model and parameter uncertainties, *wd(t)* can be entirely attributed to precipitation error, which is the focus of this work.

$$wd(t) = [Q_{obs}(t) - Q_{simu}(t)] \times \Delta t \tag{18}$$

The subscripts obs and $simu$ refer to observed and simulated discharge, respectively. The strategy for the inverse rainfall correction (IRC) using hydrograph analysis is to follow the trajectories available from the Lagrangian tracking backward from the basin outlet to the source locations at time t_i and apply a correction at the source locations proportional to the original QPE magnitude to reduce wd at time t. Detailed formulas with a conceptual drawing can be found in Appendix A. The embedded assumption is that larger QPE values have larger uncertainties. Note that QPE corrections that happened earlier in time will have an impact on runoff simulation at future times, and this is the reason why the IRC framework is a recursive framework. The detailed rainfall correction steps can be found in (Liao and Barros, 2022).

2.3.9 Methods for Reducing Uncertainties from Other Sources

As briefly mentioned before, uncertainties from other sources (e.g., model physics, model numerical formulation, antecedent soil moisture conditions, etc.) impact travel time distributions and simulated streamflow to a higher or lesser degree depending on location, antecedent conditions, and storm system. Previous studies demonstrate that, for flood-producing events in small headwater basins, streamflow response is largely controlled by precipitation inputs (e.g., Iwasaki et al., 2020). In this section, we briefly describe the methods used to minimize the impacts from other sources to enhance water budget closure using the IRC approach.

As discussed in the Introduction DCHM has been used in the Appalachian Mountains at event-scale (e.g., Tao and Barros, 2013, 2014, 2018 and 2019; Tao et al. 2016) and at seasonal and interannual scales (Yildiz and Barros 2005, 2007 and 2009), and thus extensive analysis of parameter uncertainty and model structure uncertainty has been conducted previously. Recent improvements to the flood routing algorithm have resulted in significant improvements in flood peak timing in headwater basins to reconcile the hydraulics of flood wave propagation on steep slopes at the highest elevations with milder slopes at intermediate elevations in the valleys (Liao and Barros, 2025a). Their results also suggest meandering effects, riverbank storage, and initial soil moisture distributions can impact the early rising period of the hydrographs. Significant and consistent improvements are made when introducing an initial condition correction (ICC) module to reduce initial condition uncertainty (Liao and Barros, 2025b). This innovative ICC module is coupled with the IRC framework. The red arrows in Figure 3e indicate where ICC is executed in the general architecture of the IRC framework, and the specifics of the ICC module are described below.

Particles launched during the IRC process that reached the outlet at time t are traced back directly to the IC timing or time 0, and their locations at the IC timing are shown in the bottom maps in Figure 3d (referring to control points of time t). The downstream area of the control points has shorter transportation time to arrive at the outlet (e.g., water difference ΔS_1), and the upstream area of the control points takes longer to get to the basin outlet (e.g., water difference ΔS_2). Similarly, soil moisture in the impacted area can greatly impact the size of ΔS_2 and flow conditions after the timing t_2. Assuming initial conditions are only impactful during the early period and late recession of the hydrograph, which is supported by the fact that these events are flood-producing events with large QPE uncertainties dominating the vicinity of peak flow, ICC is used for hydrological windows outside the peak flow windows. Following the same notation (backward-in-time) in the IRC framework (Eq. 18), $wd(t)$ is calculated as the flow volume difference between observed and simulated streamflows for the time interval defined by t and $t-\Delta t$. A ‘band’ of region can therefore be identified, that is, a region formed by control points of time t and control points of time $t-\Delta t$. This ‘band’ is then referred to as the impacted area of initial soil moisture for time t, meaning basin discharge between time $t - \Delta t$ and time t is impacted by initial soil moisture at the delineated impacted area. Finally, $wd(t)$ is then converted to soil moisture content and added to initial soil moisture within the impacted area (i.e. the 'band') and the details can be found in Liao and Barros (2025b).

2.3.10 Hydrological Skill Metrics

The Kling-Gupta Efficiency (KGE) is calculated using observed and simulated streamflow statistics at observation resolution τ (here 15 minutes) in this work:

$$KGE_{\tau} = 1 - \sqrt{(r-1)^2 + (\frac{\sigma_{sim}}{\sigma_{obs}} - 1)^2 + (\frac{\mu_{sim}}{\mu_{obs}} - 1)^2} \tag{19}$$

where r is the correlation between simulations and observations, σ_{obs} is the standard deviation of observed discharge, σ_{sim} is the simulated discharge standard deviation, μsim and μobs represent the average simulated and observed streamflow values, respectively.

The relative volume error (EV) is the relative difference between simulated flood volume and observed flood volume:

$$\mathrm{EV} = \frac{V_{sim} - V_{obs}}{V_{obs}} \tag{20}$$

Where V stands for volume of the flood. An EV>0, and an EV<0 mean overestimation and underestimation, respectively.

EPT refers to the error in peak flow timing between observations and simulations. For its calculation, only the highest peak is selected for calculating EPT if more than one peak is present. In this work, EPT is determined by considering the entire flood rising limb to account for the steepness of the rising limb, specifically, both the flood starting timing and the maximum flood timing from the flood front rising limb are used for calculating the EPT.

EPV or error in peak volume (Qmax, cubic meters per second) is a relative error calculated using peak flows from observations and simulations, and the equation is below:

$$\mathrm{EPV} = \frac{Qmax_{sim} - Qmax_{obs}}{Qmax_{obs}} \tag{21}$$

2.3.11 Study Domain and Model Setup

An initial 30 gauged headwater basins with areas and quality streamflow records were identified from south to north along the Appalachian Mountains (Figure 4, Table 3). Basin01 and Basin30 are over 2,000 km apart, with diverse weather and climate regimes, and large differences in geomorphology and hydrogeology. The smallest basin (Basin 07) and the largest basin (Basin 12) were discarded because their areas were less than 20 km^2 and greater than 600 km^2 , respectively due to being too small for IRC at 250 m resolution and too large for IRC due to complex hydrologic response from different catchments not all impacted by the same rainfall event. Note that an additional 2 basins (Basin 13 and 14) were later discarded from inclusion in the final data set as explained in Section 3.2 and Section 3.2.1. Therefore the final published StageIV-IRC product includes 215 events in 26 basins.

<Figure 4 here please>

Soil-related parameters were downloaded from a global high-resolution (1 km) soil data repository (Zhang et al., 2018). For each basin, the vertical hydraulic conductivity remains the same for the entire soil column. The lateral hydraulic conductivity in the unsaturated zone was assumed to be two to three orders of magnitude larger than the vertical conductivity in the shallow soil layers, with higher values where the stone fraction in the soils is higher (Carlson, 2010; Freeze and Cherry, 1979). The final scaling factors were obtained through simple sensitivity analysis to match the curvature and slope of the observed subsurface runoff recession curves (e.g., Linsley et al., 1982; Chen and Kumar, 2001; Yildiz and Barros, 2007), and scaling factors are finally determined as: 1500, 150, 15 and 1.5 for layer 1 (0-10 cm below terrain surface), layer 2 (10-75 cm below terrain surface), layer 3 (75-200 cm below terrain surface) and layer 4 (2-20 m below terrain surface), respectively. No parameter optimization is done in this work, as the primary focus of this work is to develop a QPE dataset that can consistently close the water budget while controlling uncertainties from other sources, largely advancing the understanding of QPE uncertainties across climate, weather, and geomorphological regimes.

Flood-producing events were selected for headwater basins with areas ranging between 50-500 km^2 (Table 3) for recent years from January 2021 to April 2024. A qualified event is determined based on the observed peak flow, which must surpass 95% of available flow measurements for each basin. The choice of 95% is a compromise because 99% would yield too few events, while 90% would be too close to the annual flood. Additionally, rainfall runoff response time must be shorter than or equal to 6 hours to be qualified as a flash flood event. Only warm season precipitation events from 2021 to 2024 are finally considered. Here, the warm season is specifically defined as from April 1st to September 30th. Note: data quality control is enforced, and events with missing streamflow records are discarded.

For the Cataloochee Creek Basin (Basin05), located in the SAM known to have experienced multiple flash floods in the past (Tao and Barros, 2013 and 2014), Liao and Barros (2023) created a Historical Flood Record database (HFR) that includes a large number of extreme rainfall events from 2008 to 2017. The event selection criteria when developing HFR also use the same 95% flow threshold method. The difference is that the HFR also includes multiple winter-time liquid precipitation events that result in cold-season flash floods. In total, there are 54 warm-season events for Basin 05 in HFR, and these events are also used to expand the study sample size in this work.

To initialize the DCHM, a traditional spin-up approach is used with iterative runs for the hydrological year of 2021 (from the end of April to the end of September), and it generally reaches equilibrium after 3-5 iterations. Subsequently, DCHM is continuously running from the beginning of October 2021 onwards, to derive initial conditions for events after September 30th, 2021. During this spin-up process, no parameter calibration is involved. The initial conditions are extracted from the last iteration of spin up run, and the following model outputs generated after October 1st, 2021.

2.4 Caveats

In the entire study domain, rain gauges are only installed in the Southern Appalachians, specifically in the vicinity of the Cataloochee Creek Basin (Basin 05). However, the rest of the regions are not equipped by raingauge networks, and therefore, no rain gauge bias correction is done for those basins, and the downscaled original dataset StageIV (i.e., $STIV_D$) is used as input for the IRC method and hydrological simulations in this study.

As an important component of the IRC framework, the Lagrangian tracking algorithm is only implemented when hydrological window changes, rather than following model temporal resolution (i.e., 5 minutes), due to practical computational constraints. Additionally, we do not differentiate peak flow points and recession inflection points between simulations and observations when classifying hydrological flow regimes/windows, and consistently use observations delineate hydrological windows simply because 1) particle locations are inherently much more uncertain when simulation time is getting longer partially due to numerical truncation errors and grid-based abruptly-changing velocity fields used in the Lagrangian tracking algorithm, and 2) the computational costs of the tracking algorithm. Very short travel times (i.e., <15 minutes) are ignored because of temporal resolution restrictions from streamflow observations. A systematic use of 24 hours for event total duration is imposed in this work to reduce excessive tracking workload, which might be problematic for events with very long and heavy tails, though not common for flash flood events in headwater basins.

The IRC-ICC recursive framework allows us to quantify QPE uncertainties more realistically by improving initial soil moisture estimation, and this framework is numerically efficient in terms of reaching hydrological equilibrium state within 3-5 iterations. In this work, the stable state of IRC-ICC is reached when the KGE changes are bound by 0.05.

3. Results and Discussion

3.1 Rain gauge Bias Correction

The climatologically corrected $\text{STIV}_{\text{DBKC}}$ fields have a significantly accurate diurnal cycle compared to only event-scale bias-corrected STIV_{DBK}. This process is illustrated in Figure 5 for one rain gauge from each side of the ridges (eastern side: left panel; western side: right panel) in the Southern Appalachians.

<Figure 5 here please>

Original StageIV$_D$ show higher biases over the western ridges (e.g., right panel) for all hours of day, illustrating the difficulties of capturing seeder-feeder enhancement of low-level precipitation systems (Duan and Barros, 2017). Also, the mid-day dry bias has been a problem for radar measurements in this region. (e.g., Barros and Arulraj, 2019). Results show that StageIV$_{DBKC}$ datasets capture precipitation climatology better with smaller missing detection errors compared to original StageIV. Figure 6 shows the diurnal characteristics of the missing percipitataion for two raingauge locations for winter season (January-February and March – JFM) using StageIV, and this phenonemon is observed for both the StageIV$_D$ (black) and StageIV$_{DBK}$ (cyan). These missing cases correspond to light rainfall that have small rainfall measurements at rain gauge locations (< 1.5 mm/hr, bottom row). After applying precipitation climatology corrections, the missing issue in StageIV$_{DBK}$ is significantly alleviated and much better results are shown in StageIV$_{DBKC}$ fields (green).

<Figure 6 here please>

The seasonal HSS, TS, and RMSE of STIV$_{DBKC}$ are significantly better than those of STIV$_D$ throughout the day using 10-year averages (Figure 7a). It is worth noting with increasing precipitation rate threshold (Figure 7b), threat score does not show decreasing trend, meaning raingauge bias correction for heavy rainfall events works well. Figure 7c shows RMSE performance conditional on rain rate at diurnal and seasonal scales. Overall, the RMSE is generally less than 0.1 mm/hr except in the cold-season morning and late afternoon, which can be partially attributed to snow events because these raingauges are not heated.

<Figure 7 here please>

3.2 Hydrologic Correction

The coupled IRC-ICC was originally developed and applied in Basin 05, the Cataloochee Creek Basin, and an example showing the results from iterations is demonstrated in Figure 8. The notation follows the definition in Figure 3. Note that the $\mathrm{STIV_{DBKC}}$ data derived in Section 3.1 are further downscaled to 250m and used for hydrological simulations in this section. For all other basins (except Basin05), rain gauges are not available, and $\mathrm{STIV_{D}}$ data are used instead.

<Figure 8 here please>

It is demonstrated that IRC-ICC produces stable results after about 3 to 4 iterations without significant oscillations for this specific extreme flood event. In general, for less significant events, IRC-ICC reaches equilibrium faster (merely three iterations), providing fast and convergent corrections. As explained earlier, the equilibrium state is reached and thus IRC-ICC is stopped when oscillations in simulated KGE are within 0.05, and then IRC-ICC is stopped immediately. This study suggests that for most events, three iterations is a good rule of thumb. The difference between the initial 4D (x, y, z, t) rainfall forcing and the final result of the IRC-ICC is the general IRC correction.

3.2.1 Systematic Application of IRC-ICC

The IRC-ICC is systematically executed in the 28 basins located in the Appalachians for 225 events, and examples are displayed in Figure 9.

<Figure 9 here please>

Simulated streamflows generally have better performances in the Northern and Southern Appalachian Mountains (NAM, SAM) compared to the Central (CAM). Specifically, in the Karst region along the interstate border of Virginia and West Virginia in the CAM, for Basins 13 and 14, where there are numerous caverns and natural tunnels facilitating fast subsurface flow response, that is, sinking and subterranean streams (https://www.dcr.virginia.gov/natural-heritage/vacavetrail and https://docslib.org/doc/2284608/west-virginia-tax-districts-containing-karst-terrain). The current version of the DCHM does not have a specific module designed for karst geology and karst hydrological processes. Thus, the IRC-ICC results in these locations are impacted by model structural uncertainty. Here, the advantage of not calibrating model parameters becomes apparent. It would be possible to calibrate model parameters to improve model simulations; however, the physical basis and transferability of the IRC-ICC results would be compromised. The 10 events in Basins 13 and 14 are therefore discarded (example: Figure A4). This point of discussion is highlighted here to reinforce the value of the data set presented in this manuscript for applications with other hydrologic models, including model calibration, where model structural uncertainty is not a primary concern at resolved scales.

Event 2021-06-10 in Basin 19 (see Figure A4) is an example of an event with a complex hydrograph (e.g., multiple minor flood peaks around one major flood peak) that requires more hydrological windows (see Figure 3). Subtle changes in the hydrograph shape could be indicative of spatial shifts in runoff production from one tributary to another following the track of storm cells over the basin. Indeed, depending on the weather system and regional topography, the travel velocity of such cells and their life-cycle may require finer spatial and temporal resolution both for the hydrological model and for the tracking algorithm to capture changes in the spatial structure of precipitation, especially in the case of summer thunderstorms. For the systematic production of this data set, a 5-window IRC-ICC framework was applied, including a pre-rising-point segment, rising limb, early recession, and late recession (separated by the recession inflection point).

3.2.2 IRC and IRC-ICC Precipitation Corrections

Accumulated rainfall totals per rainfall event are calculated for both the IRC-only product and post IRC-ICC products. Subsequently, these rainfall totals are directly compared against original product $\mathrm{STIV}_{\mathrm{DBKC}}$. Examples are shown in Figure 10, categorized by seasons in the Cataloochee Creek Basin (Basin05). Again, the warm season is defined as April 1st to September 30th, and the remaining events are defined as the cold season, with only liquid precipitation events studied in this work.

<Figure 10 here please>

The original QPE (**a1** and **b1**) shows abrupt changes in rainfall intensity, which is a common issue of radar observations at high spatial resolution. On the contrary, the IRC-corrected precipitation maps demonstrate precipitation features aligning with landform, showing strong spatial precipitation gradients along ridges and adjacent valleys (examples are listed in Figure A3). The spatial correlation between orographic precipitation and topography is observed across all mountain ranges, including the Appalachians (e.g., Konrad II, 1994; Smith et al., 2011; Wolvin et al., 2024). Note the dark blue colors in Figure 10 corresponding to very low precipitation near the basin outlet are an artifact of the IRC tied to very short travel times that cannot be fully resolved even at fine scales of 250m and 5minutes. However, these artifacts are much reduced for the IRC-ICC due to the reduction of uncertainty in initial conditions, as shown for the 2009-10-14, 2009-04-20, and 2013-04-12 events because of overall basin-wide travel time improvement. It is worth noting that these three events are relatively mild events, indicating a larger impact of IC on relatively less extreme events because of the critical role of IC in runoff generation mechanisms and travel times distributions. Thus, the extreme event precipitation product obtained from IRC-ICC is the data set recommended for applications with other hydrologic models.

3.2.3 Precipitation and Hydrologic Skill Metrics

Event-total precipitation maps are calculated for each basin and event, and basin-scale precipitation statistics (e.g., mean and standard deviation) are derived for each event-total precipitation map. These statistics are plotted in Figure 11, and subregions are separated by vertical black lines. Basins 01 to 11 are located in the SAM, Basins 12 to 20 are located in the CAM, and Basins 21 to 30 are located in the NAM. Basins 13 and 14 are not included in the statistics.

<Figure 11 here please>

It is clearly demonstrated that the change in the mean (i.e., basin-averaged event total QPE) is relatively small (from 36.10mm to 38.07mm) compared to the change in the standard deviation (from 6.63mm to 14.08mm) after the application of IRC-ICC. The small standard deviation of the original QPE suggests that the original QPE data are spatially tightly clustered with low variability (see Figure 10a for boxy rainfall features), while the larger standard deviation post-IRC-ICC indicates spatial variability is enhanced, which is highlighted by the terrain-aligned precipitation features in Figure 10c. The relatively small change in the mean indicates that the original input precipitation (i.e., StageIV$_{DBKC}$ for Basin 05, and StageIV$_{D}$ for the remaining basins) does not contain significant unconditional systematic biases across basins and events, which would lead to consistent positive or negative flood volume errors. As an exception, it is worth noting that the standard deviation of Basin 05 events does not change significantly after the IRC-ICC compared to other basins and events because rain gauge corrections from the IPHEx network are employed in Basin 05 but not anywhere else. It can never be overly emphasized that even after rain gauge bias correction, essentially a point-scale correction method, the resulting flood hydrograph exhibits significant water budget closure errors (see Figure 12 for more discussion) on account of the high heterogeneous nature of QPE in complex terrain.

The hydrologic statistics described in Table 1 using all studied events are plotted in Figure 12.

<Figure 12 here please>

Figure 12 shows that the median KGE across events is improved from 0.36, 0.39, 0.27 to 0.89, 0.74, 0.84 for SAM, CAM, and NAM, respectively. It should be pointed out that QPE changes for Basin 05 events (event numbers 55 to 108) are important for improving water budget closure, albeit small in magnitude compared to other events in other basins, as shown in Figure 11 and 12, and yet critical to capture the complex precipitation heterogeneity in complex terrain to close the water budget. The results for Basin 05 illustrate the limitations of rain gauge-based bias corrections in complex terrain in general. The relatively small improvement shown in the CAM is partially attributed to the fact that DCHM does not have a proper representation of subterranean rivers in karst terrain, causing large baseflow errors during hydrograph recession and thus low KGE values. Nevertheless, for flash flood applications, peak flow magnitude, flood flow timing, and event flow volume are the most important forecast objectives, corresponding to the 2nd, 3rd, and 4th horizontal panels in Figure 12. Overall, flood volume error (EV) is controlled within ±10% for over 90% of the studied events (the 2nd panel), with the median EV error being less than 5% in the SAM and NAM after IRC-ICC corrections. Flood peak volume (the 3rd panel) is generally controlled within 20%, which is very good for extreme events in regions without ground-based observations except for radars placed far away. This is demonstrated by Tropical Storm Fred on 2021-08-17: an event that caused floods in multiple SAM basins, caused five deaths, and resulted in an economic loss of more than 1 billion dollars. Note the KGE for this event is improved to 0.9, and peak timing errors are <30 minutes using IRC-ICC. Timing errors (shown in the 4th subplot) are bounded by ±60 minutes for the major of the events for post IRC-ICC datasets, though some outliers exist potentially due to complex antecedent land surface physics (e.g., rain on snow) for April events, particularly in the CAM and NAM.

Events associated with significant timing errors (more than ±90 minutes) are investigated in detail. These include the 2023-07-08 event (event number 185) for Basin 27, which is located in New Hampshire (the estimated flood front occurs too early by 2.5 hours). This was a localized summer thunderstorm event, only taking 30 minutes to reach its peak flow. The fast changes in the hydrological regime require much more windows than the current classic 5-window settings used in the IRC-ICC framework. The event on 2022-05-27 (event number 118) in Basin16 located in West Virginia is characterized by a slow rising limb. Note Basin16 is partially located in a complex region with karst features (e.g., sink holes) in the Greenbrier-river valley. Finally, the event 2021-09-22, a complex rainfall system characterized by multiple rain cells passing through the Basin 19 quickly (event number 133), requiring smaller hydrological windows to capture highly variable rainfall-runoff responses than the 5-window default IRC-ICC architecture: baseflow segment, pre-rising segment, flood rising limb, early and late recession.

Overall, large improvements in QPE are achieved, resulting in hydrological improvements in aspects of peak magnitude, flood total volume and flood front timing. Due to the dependence of IRC-ICC on travel time distributions, it cannot be used when precipitation is missing or there are severe timing errors because of the lack of water travel time trajectories to distribute corrections. From a practical point of view, the QPE IRC-ICC correction is in nature a type of space-time bias correction. The improved QPE data facilitates the development of QPE error models, which is demonstrated by the same authors (e.g., Liao and Barros, 2023), providing a path towards correcting remote-sensing products to support hydrometeorological studies and advancing the calibration of hydrological models with significantly less forcing uncertainty.

3.2.4 Independent Verification

As mentioned in the introduction, precipitation measurements are limited in the Appalachians except for the IPHEx rain gauge network (Figure 1). Currently, the NEXRAD radar network remains the widely used precipitation monitoring system in this region in spite of well-documented low radar quality coverage over radar gaps in the mountains. The Multi-Radar/Multi-Sensor (MRMS) product (Zhang et al., 2016), which is developed using NEXRAD radar measurements similar to StageIV, is created at 1km resolution and is used here for independent verification.

First, original MRMS data are downscaled to the same resolution as StageIV$_D$ datasets (250m, 5min) and used as inputs for DCHM. Hydrological simulations in this section are using the same model configuration and initial model states for the purpose of a meaningful comparison, including the following datasets: MRMS$_D$, StageIV$_D$, and IRC-ICC StageIV$_D$ as shown in Figure 13. Figure 13a shows that MRMS and StageIV QPE have similar results. Second, the IRC-ICC StageIV$_D$ have generally a good agreement with MRMS$_D$ similar to StageIV$_D$. However, for some cases, where rainfall is dramatically underestimated by the radar system and KGE values are low, IRC-ICC is shown to provide effective corrections. Otherwise, the IRC-ICC generates physically constrained corrections spatially (see Figure 10), achieving high KGE values for flood simulations. Figure 13b shows the histogram of the KGE values across different rainfall products for all events. Overall, simulated streamflows using MRMS$_D$ and StageIV$_D$ exhibit similar hydrologic performance (the median KGE across events is close to 0.20), on the contrary, post-IRC-ICC StageIV$_D$ produce flood simulations with a median KGE above 0.80.

4. Discussion and Future Work

Limitations in this study stem mainly from computational constraints rather than methodology. A default 24-hour flood duration window is imposed, implying that for long-lasting floods, due to significant slow interflow and baseflow contributions, are not considered. The current version of the IRC-ICC framework was built to support flash flood studies and only targets shallow subsurface moisture transport, given the critical importance of shallow soil moisture on the regulation of flood generation and propagation in steep terrain. It is worth noting that for long-lasting rainfall events or regions with relatively flat terrain, slow interflows would become more important in terms of regulating flood timing, flood volume, and post IRC-ICC QPE.

While the IRC results could be further optimized if carried out at the same frequency as the model resolution, therefore eliminating any artifacts due to inadequate sampling and updating of travel time distributions, and while there is room to improve the IRC-ICC framework through improved model physics and resolution, utilizing 3D velocity fields to capture the full travel time distributions, and using different models to generate IRC ensembles. to test and calibrate hydrologic models for an intercomparison study, advancing flood forecasting skill, and to support emergency management response.

5. Data Availability Statement

The StageIV-IRC dataset at 250 m 5-minute resolution for 26 basins and 215 events is available at: https://doi.org/10.5281/zenodo.14028866. (Liao and Barros, 2025c), excluding Basin 07 (the smallest basin), 12 (the largest basin), 13 (Karst terrain), and 14 (Karst terrain) based on previous discussion. Associated geographic documentation of the selected basins is also provided via the same link. Initial soil moisture distributions for the studied events are also available in the same Zenodo repository.

6. Conclusion

QPE has been an enduring challenge in hydrology, particularly in complex terrain. Ground-based radar QPE is plagued with uncertainties from multiple sources, while rain gauge networks are scarce and suffer from the lack of representativeness in the mountains. To address this grand challenge, we develop a series of corrections from point-scale to watershed-scale encompassing event bias, climatology, and water budget closure: the IRC-ICC framework. To our knowledge, this is the first QPE dataset that meets standard statistical evaluations against point-based measurements where available and meets water budget closure at flood-event scale, consistent with nonlinear rainfall-runoff processes in headwater basins, and achieves superior hydrological performance at sub-hourly.

The IRC-ICC framework is successfully adopted in 26 mountainous basins (excluding the basins that are heavily overlapped with Karst terrain) in the Appalachians for 215 events with robust success, yielding substantial improvements of streamflow simulation, particularly in terms of flood volume and timing. The tracking algorithm in the IRC-ICC framework is only updated when shifting from one hydrological window to another, but not every time step. With enough computational resources, post-IRC-ICC QPE data should further improve by capturing transient travel time distributions between model time steps.

When using the StageIV-IRC product, flood timing errors are controlled with one hour for 90% of events, compared to less than 20% when using original StageIV, while the median KGE improved from 0.34 to 0.86 across the events. This change in KGE is achieved by significant changes in the space-time variance of precipitation that in turn impacts the space-time variability of rainfall-runoff processes. Results illustrate the importance of initial conditions for less severe rainfall events, particularly during the beginning of the event, which influences subsequent streamflow simulations. It should be emphasized that physical parameters are not calibrated for any precipitation event in any basin in this work. This physics-based IRC-ICC framework can capture the fundamental physics involved in flash flood events: essentially the fast rainfall-runoff responses in surface and shallow subsurface layers; therefore, skillful hydrologic prediction is achieved without model calibration. Instead, the focus is on getting the forcing right.

The IRC-ICC is a general framework that can be incorporated into any distributed hydrological model. Thus, the StageIV-IRC dataset also enables meaningful intercomparison among different radar QPE datasets, providing physics insights into QPE error structure from a water budget closure perspective, toward improving radar retrievals and to characterize radar-specific errors related to radar operations at high spatial resolution in the mountains. The demonstrated success of StageIV-IRC in ungauged basins strongly supports the use of IRC-ICC in mountainous regions worldwide, where rain gauges are generally not available. Further, this dataset can be utilized as a reference for building machine learning models (or even deep-learning models when the number of studied precipitation events is expanded) that can learn the QPE uncertainties conditional on time of day, weather, climate and geomorphological regimes for both radar QPE analysis and forecasts, advancing the understanding and quantification of orographic precipitation uncertainty at high resolution across global mountains.

7. Appendix A

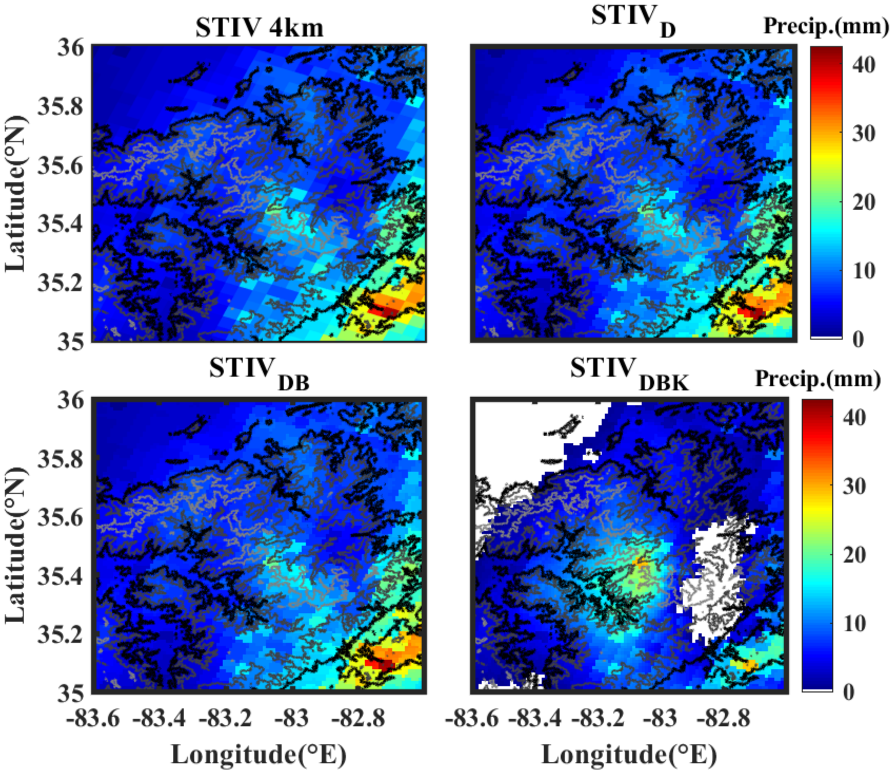

Figure A1 - Spatial rainfall fields on 2014-05-15, 06-07 UTC. Rain rates between 0 to 1mm/h are mapped in white.

The detailed distribution process of water difference (wd) is illustrated in Figure A2 following Section 2.3.8.

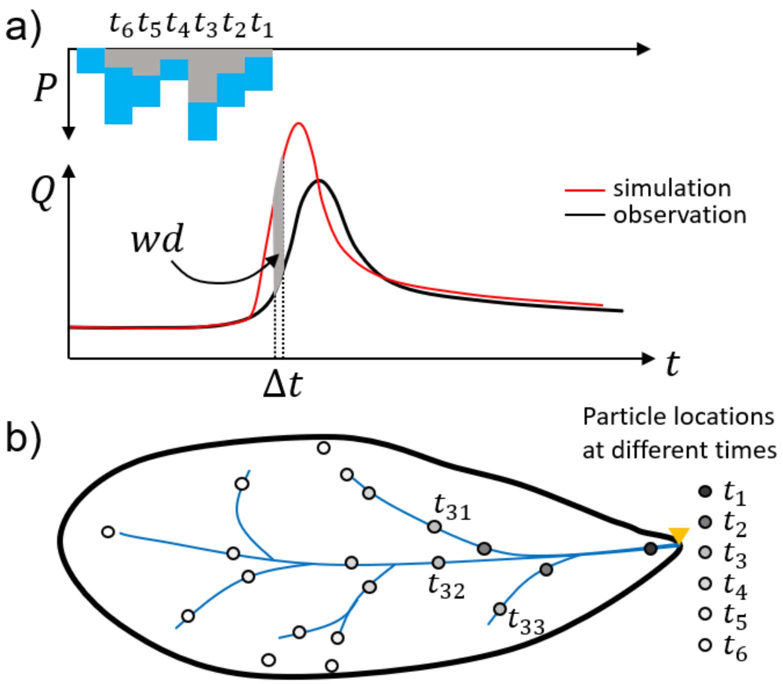

c)

$$wd_3 = wd \cdot \frac{P_3}{P_1 + P_2 + \cdots + P_n}$$

$$\Delta P_{31} = wd_3 \cdot \frac{P_{31}}{P_{31} + P_{32} + P_{33}}$$

$$P_{31}^{new} = P_{31} + \Delta P_{31}$$

Figure A2 - Schematic depiction of the IRC framework and key mathematical equations. Panel **(a)** illustrates the nonlinear relationship between streamflow and precipitation, where wd represents the residual between discharge simulations and observations at the basin outlet. The variation of precipitation in the basin as a function of time is shown by the basin hyetograph in blue. The hyetograph time series (blue) spans the duration of the precipitation event between t_1 to t_n. In gray is the hyetograph over the area of interest for panels (b) and (c). To map the streamlines, water particles are launched every time step and their trajectory to the outlet is tracked and saved. Panel **(b)** shows the source areas of water particles launched at various time steps ($t_1, t_2, \ldots\ t_6 \ldots$) from all locations where runoff is produced, and the particles are tracked until they eventually reach the basin outlet. The streamlines of particles that reach the outlet at the same time are used to distribute the residuals backwards to the runoff source areas where the particles were originally launched (e.g., the three particles t_{31}, t_{32}, and t_{33} that reach the basin outlet at time t_3). Panel **(c)** shows the algorithm to calculate the rainfall bias correction at location t_{31} due to the residual wd_3 at time t_3. P_i is basin averaged rainfall at time t_i, and wd_3 is the runoff volume to be corrected at time step t_3. ΔP_{31} is the precipitation correction for pixel t_{31}, and precipitation amount at pixel t_{31} before and after IRC are denoted by P_{31} and P_{31}^{new}. This figure is adapted from Liao and Barros (2025b).

A zoom in map of the Southern Appalachians is plotted associated with DEM maps of other basins. A complete set of maps for each individual basin can be requested. Note, the rain gauges used in this study are plotted in Figure 1, and they are primarily near Basin05.

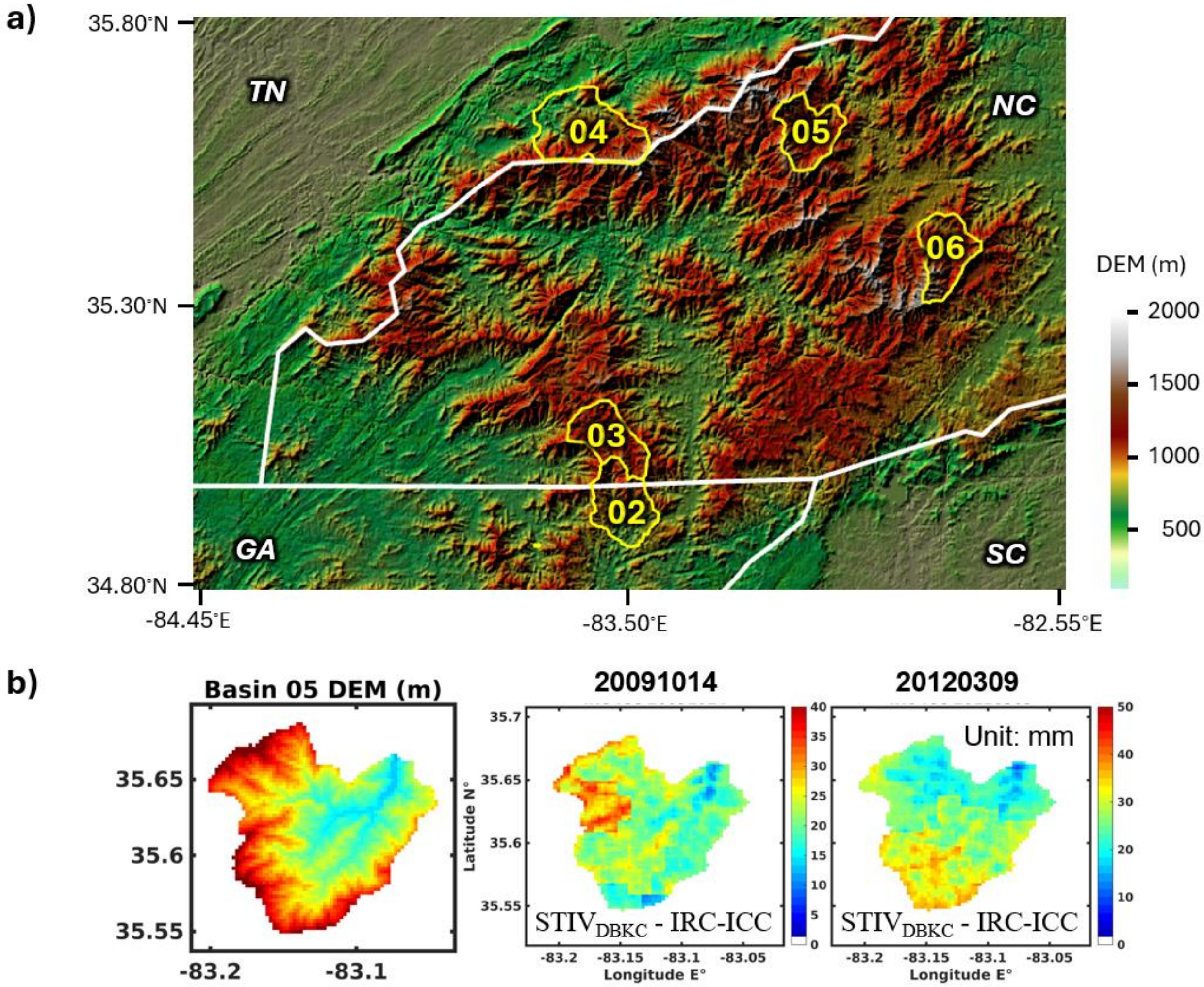

Figure A3 – A zoom-in map of the Figure 4 for watersheds in the Southern Appalachians (Panel a). The DEM map and examples of rainfall event accumulation of Basin 05 (Panel b) to show rainfall alignment with topography.

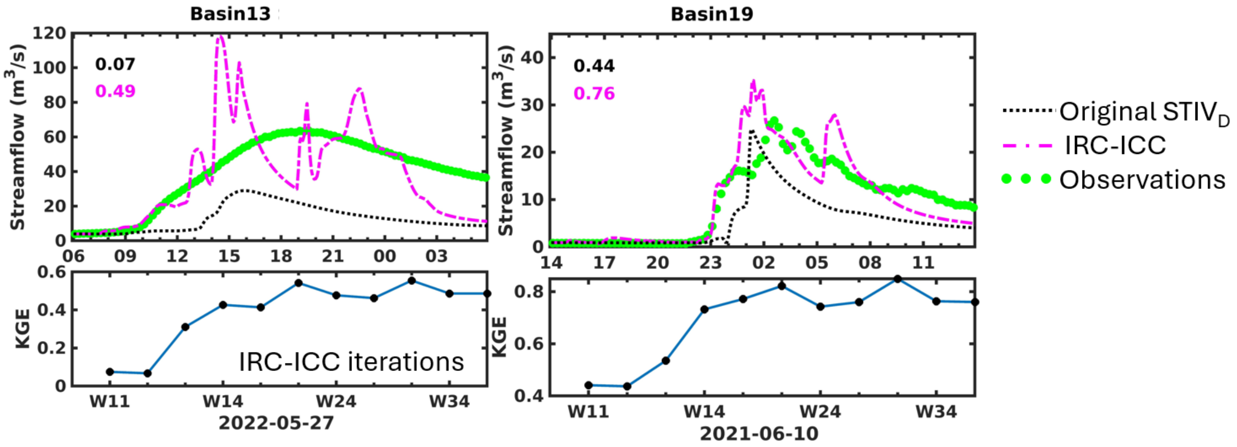

Figure A4 – Examples of the coupled IRC-ICC framework application in Basin 13 and Basin 19 for discussion in the manuscript. KGE values are displayed in the top left corners. Basin 13 is located in Karst terrain, while the event in Basin 19 is an example with a complex hydrograph.

CREDIT AUTHOR STATEMENT

M. Liao: Methodology, Data curation, Writing - original draft, Investigation. A. P. Barros: Conceptualization, Methodology, Writing - review & editing, Supervision, Project administration, Funding acquisition.

COMPETING INTERESTS

The authors declare there are no competing interests.

ACKNOWLEDGMENTS

The work was supported by NASA Earth System Science Fellowship associated with the first author and supported by a joint effort from NASA grant 80NSSC19K0685 and a grant from the IBM Accelerator program with the second author.

REFERENCES

Alimonti, G., Mariani, L., Prodi, F., & Ricci, R. A. (2022). A critical assessment of extreme events trends in times of global warming. *European Physical Journal - Plus*, 137, 112. https://doi.org/10.1140/epjp/s13360-021-02243-9

Allen, J. T. (2018). Climate change and severe thunderstorms. In Oxford research encyclopedia of climate science. https://doi.org/10.1093/acrefore/9780190228620.013.62

Andrieu, H., Creutin, J. D., Delrieu, G., & Faure, D. (1997). Use of a weather radar for the hydrology of a mountainous area. Part I: Radar measurement interpretation. *Journal of Hydrology*, *193*(1-4), 1-25.

Areerachakul, N., Prongnuch, S., Longsomboon, P., & Kandasamy, J. (2022). Quantitative precipitation estimation (QPE) rainfall from meteorology radar over Chi Basin. *Hydrology*, *9*(10), 178. https://doi.org/10.3390/hydrology9100178

Arulraj, M., & Barros, A. P. (2017). Shallow precipitation detection and classification using multifrequency radar observations and model simulations. *Journal of Atmospheric and Oceanic Technology*, *34*(9), 1963-1983. https://doi.org/10.1175/JTECH-D-17-0060.1

Arulraj, M., & Barros, A. P. (2021). Automatic detection and classification of low-level orographic precipitation processes from space-borne radars using machine learning. *Remote Sensing of Environment*, *257*, 112355. https://doi.org/10.1016/j.rse.2021.112355

Barros, A., & Arulraj, M. (2020). Remote sensing of orographic precipitation. In V. Levizzani, C. Kidd, D. B. Kirschbaum, C. D. Kummerow, K. Nakamura, & F. J. Turk (Eds.), Satellite precipitation measurement. Springer. https://doi.org/10.1007/978-3-030-35798-6_6

Barros, A., Miller, D., Wilson, A., Cutrell, G., Arulraj, M., Super, P., & Petersen, W. (2017). GPM Ground Validation Southern Appalachian Rain Gauge IPHEx [indicate subset used]. Dataset available online from the NASA Global Hydrometeorology Resource Center DAAC, Huntsville, Alabama, U.S.A. DOI: http://dx.doi.org/10.5067/GPMGV/IPHEX/GAUGES/DATA301

Barros, A.P., Petersen, W., Schwaller, M., Cifelli, R., Mahoney, K., Peters-Liddard, C., Shepherd, M., Nesbitt, S., Wolff, D., Heymsfield, G. & Starr, D. (2014) NASA GPM-Ground Validation: Integrated Precipitation and Hydrology Experiment 2014 Science Plan. EPL/Duke University: Durham, N.C. https://doi.org/10.7924/G8CC0XMR.

Berndt, C., Rabiei, E., & Haberlandt, U. (2014). Geostatistical merging of rain gauge and radar data for high temporal resolutions and various station density scenarios. *Journal of Hydrology*, *508*, 88-101. https://doi.org/10.1016/j.jhydrol.2013.10.028

Bindlish, R. and Barros, A.P., (1996): Aggregation of Digital Terrain Data Using a Modified Fractal Interpolation Scheme. *Computers & Geosciences*, 22, 907-917.

Bindlish, R., & Barros, A. P. (2000). Disaggregation of rainfall for one-way coupling of atmospheric and hydrological models in regions of complex terrain. *Global and Planetary Change*, *25*(1-2), 111-132. https://doi.org/10.1016/S0921-8181(00)00024-2

Bohling, G. (2005). Introduction to geostatistics and variogram analysis. Kansas geological survey, 1(10), 1-20.

Borga, M., Stoffel, M., Marchi, L., Marra, F., & Jakob, M. (2014). Hydrogeomorphic response to extreme rainfall in headwater systems: Flash floods and debris flows. *Journal of Hydrology*, *518*, 194-205.

Buytaert, W., Celleri, R., Willems, P., De Bievre, B., & Wyseure, G. (2006). Spatial and temporal rainfall variability in mountainous areas: A case study from the south Ecuadorian Andes. Journal of hydrology, 329(3-4), 413-421. https://doi.org/10.1016/j.jhydrol.2006.02.031

Carlson, D., (2010). Influence of lithology on vertical anisotropy of permeability at a field scale for select Louisiana geologic units. Gulf Coast Association of Geological Societies Transactions, 60: 103-118.

Cassiraga, E., Gómez-Hernández, J. J., Berenguer, M., Sempere-Torres, D., & Rodrigo-Ilarri, J. (2021). Spatiotemporal precipitation estimation from rain gauges and meteorological radar using geostatistics. *Mathematical Geosciences*, *53*, 499-516. https://doi.org/10.1007/s11004-020-09882-1

Chen, J., Kumar, P., 2001. Topographic influence on the seasonal and interannual variation of water and energy balance of basins in North America. Journal of Climate, 14(9).

Czigány, S., Pirkhoffer, E., & Geresdi, I. (2010). Impact of extreme rainfall and soil moisture on flash flood generation. *Quarterly Journal of the Hungarian Meteorological Service*, *114*(1-2), 79-100.

Deijns, A. A., Dewitte, O., Thiery, W., d'Oreye, N., Malet, J. P., & Kervyn, F. (2022). Timing landslide and flash flood events from SAR satellite: a regionally applicable methodology illustrated in African cloud-covered tropical environments. *Natural Hazards and Earth System Sciences*, *22*(11), 3679-3700. https://doi.org/10.5194/nhess-22-3679-2022

Delrieu, G., Wijbrans, A., Boudevillain, B., Faure, D., Bonnifait, L., & Kirstetter, P. E. (2014). Geostatistical radar–rain gauge merging: A novel method for the quantification of rain estimation accuracy. *Advances in Water Resources*, *71*, 110-124. https://doi.org/10.1016/j.advwatres.2014.06.005

Diggle, P. and Ribeiro, P. J., 2007. Model-based geostatistics. Springer Series in Statistics, 230.

Dinku, T., Anagnostou, E. N., & Borga, M. (2002). Improving radar-based estimation of rainfall over complex terrain. Journal of Applied Meteorology and Climatology, 41(12), 1163-1178. https://doi.org/10.1175/1520-0450(2002)041<1163:IRBEOR>2.0.CO;2

Diomede, T., Davolio, S., Marsigli, C., Miglietta, M. M., Moscatello, A., Papetti, P., ... & Malguzzi, P. (2008). Discharge prediction based on multi-model precipitation forecasts. *Meteorology and atmospheric physics*, *101*, 245-265. https://doi.org/10.1007/s00703-007-0285-0

Dobler, C., Hagemann, S., Wilby, R. L., & Stötter, J. (2012). Quantifying different sources of uncertainty in hydrological projections in an Alpine watershed. *Hydrology and Earth System Sciences*, *16*(11), 4343-4360. https://doi.org/10.5194/hess-16-4343-2012

Duan, Y., Wilson, A.M., and Barros, A.P., 2015: Scoping a Field Experiment: Error Diagnostics of TRMM Precipitation Radar Estimates in Complex Terrain as a basis for IPHEx2014. *Hydrol. Earth Sys. Sci.*, 19,1501-1520.https://doi.org/10.5194/hess-19-1501-2015.

Duan, Y., & Barros, A. P. (2017). Understanding how low-level clouds and fog modify the diurnal cycle of orographic precipitation using in situ and satellite observations. *Remote Sensing*, *9*(9), 920. https://doi.org/10.3390/rs9090920

Durden, S. L., Haddad, Z. S., Kitiyakara, A., & Li, F. K. (1998). Effects of nonuniform beam filling on rainfall retrieval for the TRMM precipitation radar. Journal of Atmospheric and Oceanic Technology, 15(3), 635-646. https://doi.org/10.1175/1520-0426(1998)015<0635:EONBFO>2.0.CO;2

Foresti, L., & Pozdnoukhov, A. (2012). Exploration of alpine orographic precipitation patterns with radar image processing and clustering techniques. Meteorological Applications, 19(4), 407-419. https://doi.org/10.1002/met.272

Freeze, R.A., Cherry, J.A., 1979. Groundwater. Englewood Cliffs, N.J. : Prentice-Hall.

Fulton, J., & Ostrowski, J. (1998). Measuring real-time streamflow using emerging technologies: Radar, hydroacoustics, and the probability concept. *Journal of Hydrology*, *357*(1-2), 1-10. https://doi.org/10.1016/j.jhydrol.2008.03.028

Gentilucci, M., Bufalini, M., D'Aprile, F., Materazzi, M., & Pambianchi, G. (2021). Comparison of data from rain gauges and the IMERG product to analyse precipitation in mountain areas of central Italy. ISPRS International Journal of Geo-Information, 10(12), 795. https://doi.org/10.3390/ijgi10120795

Goudenhoofdt, E., & Delobbe, L. (2009). Evaluation of radar-gauge merging methods for quantitative precipitation estimates. *Hydrology and Earth System Sciences*, *13*(2), 195-203. https://doi.org/10.5194/hess-13-195-2009

Grillakis, M. G., Koutroulis, A. G., Komma, J., Tsanis, I. K., Wagner, W., & Blöschl, G. (2016). Initial soil moisture effects on flash flood generation–A comparison between basins of contrasting hydro-climatic conditions. *Journal of Hydrology*, *541*, 206-217.

Gupta, H. V., Kling, H., Yilmaz, K. K., & Martinez, G. F. (2009). Decomposition of the mean squared error and NSE performance criteria: Implications for improving hydrological modelling. *Journal of hydrology*, *377*(1-2), 80-91. https://doi.org/10.1016/j.jhydrol.2009.08.003

Gupta, V., Nautiyal, H., Kumar, V., Jamir, I., & Tandon, R. S. (2016). Landslide hazards around Uttarkashi township, Garhwal Himalaya, after the tragic flash flood in June 2013. Natural Hazards, 80, 1689-1707. https://doi.org/10.1007/s11069-015-2048-4

Harrison, D. L., Driscoll, S. J., & Kitchen, M. (2000). Improving precipitation estimates from weather radar using quality control and correction techniques. Meteorological Applications, 7(2), 135-144. https://doi.org/10.1017/S1350482700001468

Huffman, G. J., R. F. Adler, D. T. Bolvin, G. J. Gu, E. J. Nelkin, K. P. Bowman, Y. Hong, E. F. Stocker, and D. B. Wolff (2007), The TRMM multisatellite precipitation analysis (TMPA): Quasi-global, multiyear, combined-sensor precipitation estimates at fine scales, J. Hydrometeorol., 8(1), 38–55. https://doi.org/10.1175/JHM560.1

Iwasaki, K., Katsuyama, M., & Tani, M. (2020). Factors affecting dominant peak-flow runoff-generation mechanisms among five neighbouring granitic headwater catchments. Hydrological Processes, 34(5), 1154-1166. https://doi.org/10.1002/hyp.13656

Kim, G., & Barros, A. P. (2001). Quantitative flood forecasting using multisensor data and neural networks. Journal of Hydrology, 246(1-4), 45-62. https://doi.org/10.1016/S0022-1694(01)00353-5

Kobold, M., & Sušelj, K. (2005). Precipitation forecasts and their uncertainty as input into hydrological models. *Hydrology and Earth System Sciences*, *9*(4), 322-332. https://doi.org/10.5194/hess-9-322-2005

Kochendorfer, J., Rasmussen, R., Wolff, M., Baker, B., Hall, M. E., Meyers, T., ... & Leeper, R. (2017). The quantification and correction of wind-induced precipitation measurement errors. Hydrology and Earth System Sciences, 21(4), 1973-1989. https://doi.org/10.5194/hess-21-1973-2017

Komma, J., Reszler, C., Blöschl, G., & Haiden, T. (2007). Ensemble prediction of floods–catchment non-linearity and forecast probabilities. *Natural Hazards and Earth System Sciences*, *7*(4), 431-444.

Konrad II, C. E. (1994). Moisture trajectories associated with heavy rainfall in the Appalachian region of the United States. Physical Geography, 15(3), 227-248. https://doi.org/10.1080/02723646.1994.10642514

Kreklow, J., Tetzlaff, B., Burkhard, B., & Kuhnt, G. (2020). Radar-based precipitation climatology in Germany—developments, uncertainties and potentials. *Atmosphere*, *11*(2), 217. https://doi.org/10.3390/atmos11020217

Laiolo, P., Gabellani, S., Campo, L., Silvestro, F., Delogu, F., Rudari, R., ... & Puca, S. (2016). Impact of different satellite soil moisture products on the predictions of a continuous distributed hydrological model. *International Journal of Applied Earth Observation and Geoinformation*, *48*, 131-145. https://doi.org/10.1016/j.jag.2015.06.002

Li, J., & Heap, A. D. 2008. A review of spatial interpolation methods for environmental scientists. 11-12.

Liao, M., & Barros, A. P. (2019). The Integrated Precipitation and Hydrology Experiment-Hydrologic Applications for the Southeast US (IPHEX-H4SE) Part IV: High-Resolution Enhanced Stage IV-Rain gauge Combined Precipitation Product [Dataset]. Durham, NC: Duke Digital Repository. https://idn.duke.edu/ark:/87924/r4pc2zd75

Liao, M., & Barros, A. P. (2022). Toward optimal rainfall – Hydrologic QPE correction in headwater basins. Remote Sensing of Environment, 279, 113107. https://doi.org/10.1016/j.rse.2022.113107

Liao, M., & Barros, A.P., (2025a). Model Celerity-Discharge Behavior in Complex Terrain to Improve Orographic Quantitative Precipitation Estimation and Hydrologic Prediction in Headwater Basins. *Water Resources Research*, https://doi.org/10.1029/2024WR038446

Liao, M., & Barros, A.P., (2025b). Toward optimal rainfall – Hydrologic QPE Correction in Headwater Basins — Closing the Water Budget within Observational Uncertainty Through Correcting Initial Soil Moisture Conditions. J. *Hydrology-Reg. Studies*, https://doi.org/10.1016/j.ejrh.2025.102700.

Liao, M., & Barros, A. (2025c). StageIV-IRC – A High-resolution Dataset of Extreme Orographic Quantitative Precipitation Estimates (QPE) Constrained to Water Budget Closure for

Historical Floods in the Appalachian Mountains [Data set]. Zenodo. https://doi.org/10.5281/zenodo.14028866

Lin, Y., & Mitchell, K. E. (2005), The NCEP stage II/IV hourly precipitation analyses: Development and applications, paper presented at 19th Conference on Hydrology [Dataset], Am. Meteorol. Soc., San Diego, Calif., 9–13 Jan.

Linsley, R.K., Kohler, J., Max A., Paulhus, J.L.H., (1982). Hydrology for Engineers. Water Resources and Environmental Engineering. McGraw-Hill, New York.

Lumbroso, D., & Gaume, E. (2012). Reducing the uncertainty in indirect estimates of extreme flash flood discharges. *Journal of hydrology*, *414*, 16-30.

Maggioni, V., & Massari, C. (2018). On the performance of satellite precipitation products in riverine flood modeling: A review. *Journal of hydrology*, *558*, 214-224.

Marchi, L., Borga, M., Preciso, E., & Gaume, E. (2010). Characterisation of selected extreme flash floods in Europe and implications for flood risk management. *Journal of Hydrology*, *394*(1-2), 118-133.

McBratney, A. B., & Webster, R. (1986). Choosing functions for semi-variograms of soil properties and fitting them to sampling estimates. *Journal of soil Science*, *37*(4), 617-639.

McBride, J. L., & Ebert, E. E. (2000). Verification of quantitative precipitation forecasts from operational numerical weather prediction models over Australia. *Weather and Forecasting*, *15*(1), 103-121.

McKee, J. L., & Binns, A. D. (2016). A review of gauge–radar merging methods for quantitative precipitation estimation in hydrology. Canadian Water Resources Journal/Revue canadienne des ressources hydriques, 41(1-2), 186-203. https://doi.org/10.1080/07011784.2015.1064786

Milly, P. C. D., Wetherald, R. T., Dunne, K. A., & Delworth, T. L. (2002). Increasing risk of great floods in a changing climate. *Nature*, *415*(6871), 514-517. https://doi.org/10.1038/415514a

Mockler, E. M., Chun, K. P., Sapriza-Azuri, G., Bruen, M., & Wheater, H. S. (2016). Assessing the relative importance of parameter and forcing uncertainty and their interactions in conceptual hydrological model simulations. *Advances in Water Resources*, *97*, 299-313. https://doi.org/10.1016/j.advwatres.2016.10.008

Mtibaa, S., & Asano, S. (2022). Hydrological evaluation of radar and satellite gauge-merged precipitation datasets using the SWAT model: Case of the Terauchi catchment in Japan. *Journal of Hydrology: Regional Studies*, *42*, 101134. https://doi.org/10.1016/j.ejrh.2022.101134

Nanding, N., Rico-Ramirez, M. A., & Han, D. (2015). Comparison of different radar-rain gauge rainfall merging techniques. Journal of Hydroinformatics, 17(3), 422-445. https://doi.org/10.2166/hydro.2015.001

Nogueira, M., and Barros, A.P., (2015): Transient Stochastic Downscaling of Quantitative Precipitation Estimates for Hydrological Applications. *J. Hydrology*, No. 529, 1407- 1421. https://doi.org/10.1016/j.jhydrol.2015.08.041.

Oliver, M. A., & Webster, R. (2015). *Basic steps in geostatistics: the variogram and kriging* (Vol. 106). Cham, Switzerland: Springer International Publishing.

Penna, D., Tromp-van Meerveld, H. J., Gobbi, A., Borga, M., & Dalla Fontana, G. (2011). The influence of soil moisture on threshold runoff generation processes in an alpine headwater catchment. Hydrology and Earth System Sciences, 15(3), 689-702. https://doi.org/10.5194/hess-15-689-2011

Pielke, R. A., & Downton, M. W. (2000). Precipitation and damaging floods: Trends in the United States, 1932–97. *Journal of climate*, *13*(20), 3625-3637. https://doi.org/10.1175/1520-0442(2000)013<3625:PADFTI>2.0.CO;2

Prat, O. P., & Barros, A. P. (2010a). Assessing satellite-based precipitation estimates in the Southern Appalachian mountains using rain gauges and TRMM PR. *Advances in Geosciences*, *25*, 143-153. https://doi.org/10.5194/adgeo-25-143-2010

Prat, O. P., & Barros, A. P. (2010b). Ground observations to characterize the spatial gradients and vertical structure of orographic precipitation–Experiments in the inner region of the Great Smoky Mountains. *Journal of Hydrology*, *391*(1-2), 141-156. https://doi.org/10.1016/j.jhydrol.2010.07.013

Rafieeinasab, A., Norouzi, A., Seo, D. J., & Nelson, B. (2015). Improving high-resolution quantitative precipitation estimation via fusion of multiple radar-based precipitation products. Journal of Hydrology, 531, 320-336. https://doi.org/10.1016/j.jhydrol.2015.04.066

Schiemann, R., Erdin, R., Willi, M., Frei, C., Berenguer, M., & Sempere-Torres, D. (2011). Geostatistical radar-rain gauge combination with nonparametric correlograms: methodological considerations and application in Switzerland. *Hydrology and Earth System Sciences*, *15*(5), 1515-1536. https://doi.org/10.5194/hess-15-1515-2011

Schumacher, R. S. (2017). Heavy rainfall and flash flooding. In *Oxford research encyclopedia of natural hazard science*. https://doi.org/10.1093/acrefore/9780199389407.013.132

Shao, Y., Fu, A., Zhao, J., Xu, J., & Wu, J. (2021). Improving quantitative precipitation estimates by radar-rain gauge merging and an integration algorithm in the Yishu River catchment, China. Theoretical and Applied Climatology, 144, 611-623. https://doi.org/10.1007/s00704-021-03526-y

Sideris, I. V., Gabella, M., Erdin, R., & Germann, U. (2013). Real-time radar–rain-gauge merging using spatio-temporal co-kriging with external drift in the alpine terrain of Switzerland. *Quarterly Journal of the Royal Meteorological Society*, *140*(680), 1097-1111. https://doi.org/10.1002/qj.2188

Silvestro, F., Rossi, L., Campo, L., Parodi, A., Fiori, E., Rudari, R., & Ferraris, L. (2019). Impact-based flash-flood forecasting system: Sensitivity to high resolution numerical weather prediction systems and soil moisture. *Journal of Hydrology*, *572*, 388-402. https://doi.org/10.1016/j.jhydrol.2019.02.055

Smith, J. A., Baeck, M. L., Ntelekos, A. A., Villarini, G., & Steiner, M. (2011). Extreme rainfall and flooding from orographic thunderstorms in the central Appalachians. Water Resources Research, 47(4). https://doi.org/10.1029/2010WR010190

Špitalar, M., Gourley, J. J., Lutoff, C., Kirstetter, P. E., Brilly, M., & Carr, N. (2014). Analysis of flash flood parameters and human impacts in the US from 2006 to 2012. *Journal of hydrology*, *519*, 863-870.Tao, K., and Barros, A.P., 2010: Fractal Downscaling of Satellite Precipitation

Products for Hydrometeorological Applications. *J. Atmos. Oceanic Technol*., 27 (3), 409-427. https://doi.org/10.1175/2009JTECHA1219.1

Tao, K., & Barros, A. P. (2010). Using fractal downscaling of satellite precipitation products for hydrometeorological applications. *Journal of Atmospheric and Oceanic Technology*, *27*(3), 409-427.

Tao, J., & Barros, A. P. (2013). Prospects for flash flood forecasting in mountainous regions–An investigation of Tropical Storm Fay in the Southern Appalachians. *Journal of Hydrology*, *506*, 69-89. https://doi.org/10.1016/j.jhydrol.2013.02.052

Tao, J., & Barros, A. P. (2014). Coupled prediction of flood response and debris flow initiation during warm-and cold-season events in the Southern Appalachians, USA. *Hydrology and Earth System Sciences*, *18*(1), 367-388. https://doi.org/10.5194/hess-18-367-2014

Tao, J., Wu, D., Gourley, J., Zhang, S. Q., Crow, W., Peters-Lidard, C., & Barros, A. P. (2016). Operational hydrological forecasting during the IPHEx-IOP campaign–Meet the challenge. *Journal of hydrology*, *541*, 434-456. https://doi.org/10.1016/j.jhydrol.2016.02.019

Tao, J., & Barros, A. P. (2018). Multi-year atmospheric forcing datasets for hydrologic modeling in regions of complex terrain–Methodology and evaluation over the Integrated Precipitation and Hydrology Experiment 2014 domain. *Journal of Hydrology*, *567*, 824-842. https://doi.org/10.1016/j.jhydrol.2016.12.058

Tao, J., and Barros, A.P., 2019: Multi-Year Surface Radiative Properties and Vegetation Parameters for Hydrologic Modeling in Regions of Complex Terrain – Methodology and Evaluation over the IPHEx2014 Domain. *J. Hydrology-Reg. Studies*, 22, e100596. https://doi.org/10.1016/j.ejrh.2019.100596.

Troch, P. A., Smith, J. A., Wood, E. F., & de Troch, F. P. (1994). Hydrologic controls of large floods in a small basin: central Appalachian case study. *Journal of Hydrology*, *156*(1-4), 285-309. https://doi.org/10.1016/0022-1694(94)90082-5

Uber, M., Vandervaere, J. P., Zin, I., Braud, I., Heistermann, M., Legoût, C., ... & Nord, G. (2018). How does initial soil moisture influence the hydrological response? A case study from southern France. Hydrology and Earth System Sciences, 22(12), 6127-6146. https://doi.org/10.5194/hess-22-6127-2018

Vignal, B., Galli, G., Joss, J., & Germann, U. (2000). Three methods to determine profiles of reflectivity from volumetric radar data to correct precipitation estimates. *Journal of Applied Meteorology and Climatology*, *39*(10), 1715-1726. https://doi.org/10.1175/1520-0450-39.10.1715

Villarini, G., & Krajewski, W. F. (2010). Review of the different sources of uncertainty in single polarization radar-based estimates of rainfall. *Surveys in geophysics*, *31*, 107-129. https://doi.org/10.1007/s10712-009-9079-x

Vivoni, E. R., Entekhabi, D., Bras, R. L., & Ivanov, V. Y. (2007). Controls on runoff generation and scale-dependence in a distributed hydrologic model. Hydrology and Earth System Sciences, 11(5), 1683-1701. https://doi.org/10.5194/hess-11-1683-2007

Wang, K. H., Chu, T., Yang, M. D., & Chen, M. C. (2020). Geostatistical based models for the spatial adjustment of radar rainfall data in typhoon events at a high-elevation river watershed. *Remote Sensing*, *12*(9), 1427. https://doi.org/10.3390/rs12091427

Wang, J., & Wolff, D. B. (2010). Evaluation of TRMM ground-validation radar-rain errors using rain gauge measurements. *Journal of Applied Meteorology and Climatology*, *49*(2), 310-324.

Weiland, F. C. S., Vrugt, J. A., Weerts, A. H., & Bierkens, M. F. (2015). Significant uncertainty in global scale hydrological modeling from precipitation data errors. *Journal of Hydrology*, *529*, 1095-1115. https://doi.org/10.1016/j.jhydrol.2015.08.061

Wehbe, Y., Temimi, M., & Adler, R. F. (2020). Enhancing precipitation estimates through the fusion of weather radar, satellite retrievals, and surface parameters. *Remote Sensing*, *12*(8), 1342. https://doi.org/10.3390/rs12081342

Wernberg, T., Smale, D., Tuya, F., Thomsen, M. S., Langlois, T. J., de Bettignies, T., Bennett, S., & Rousseaux, C. S. (2013). An extreme climatic event alters marine ecosystem structure in a global biodiversity hotspot. *Nature Climate Change*, 3, 78–82. https://doi.org/10.1038/nclimate1627

Wilson, A. M., & Barros, A. P. (2014). An investigation of warm rainfall microphysics in the southern Appalachians: Orographic enhancement via low-level seeder–feeder interactions. *Journal of the Atmospheric Sciences*, *71*(5), 1783-1805. https://doi.org/10.1175/JAS-D-13-0228.1

Wolvin, S., Strong, C., Rupper, S., & Steenburgh, W. J. (2024). Climatology of orographic precipitation gradients over High Mountain Asia derived from dynamical downscaling. Journal of Geophysical Research: Atmospheres, 129(20), e2024JD041010. https://doi.org/10.1029/2024JD041010

Yildiz, O., & Barros, A. P. (2004). Climate variability, water resources, and hydrologic extremes—Modeling the water and energy budgets. In *Climate and Hydrology in Mountain Areas*, (Eds. C. de Jong, D. Collins, and R. Ranzi), John Wiley and Sons (Pub.) , 303-318. https://doi.org/10.1002/0470858249.ch20

Yildiz, O., & Barros, A. P. (2007). Elucidating vegetation controls on the hydroclimatology of a mid-latitude basin. *Journal of Hydrology*, *333*(2-4), 431-448. https://doi.org/10.1016/j.jhydrol.2006.09.010

Yıldız, O., & Barros, A. P. (2009). Evaluating spatial variability and scale effects on hydrologic processes in a midsize river basin. *Sci. Res. Essays*, *4*, 217-225. https://doi.org/10.5897/SRE.9000465

Zappa, M., Jaun, S., Germann, U., Walser, A., & Fundel, F. (2011). Superposition of three sources of uncertainties in operational flood forecasting chains. *Atmospheric Research*, *100*(2-3), 246-262. https://doi.org/10.1016/j.atmosres.2010.12.005

Zehe, E., & Blöschl, G. (2004). Predictability of hydrologic response at the plot and catchment scales: Role of initial conditions. *Water Resources Research*, *40*(10).

Zhang, J., Howard, K., Langston, C., Kaney, B., Qi, Y., Tang, L., Grams, H., Wang, Y., Cocks, S., Martinaitis, S., Arthur, A., Cooper, K., Brogden, J., & Kitzmiller, D. (2016). Multi-radar multi-sensor (MRMS) quantitative precipitation estimation: Initial operating capabilities

[Dataset]. Bulletin of the American Meteorological Society, 97(4), 621–638. https://doi.org/10.1175/BAMS-D-14-00174.1

Zhang, X., & Anagnostou, E. N. (2019). Evaluation of numerical weather model–based satellite precipitation adjustment in tropical mountainous regions. *Journal of Hydrometeorology*, *20*(3), 431-445. https://doi.org/10.1175/JHM-D-18-0008.1

Zhang, Y., Schaap, M. G., & Zha, Y. (2018). A high-resolution global map of soil hydraulic properties produced by a hierarchical parameterization of a physically based water retention model. *Water Resources Research*, *54*(12), 9774-9790. https://doi.org/10.1029/2018WR023539

Zimmerman, D. L., & Zimmerman, M. B. (1991). A comparison of spatial semivariogram estimators and corresponding ordinary kriging predictors. Technometrics, 33(1), 77-91. https://doi.org/10.1080/00401706.1991.10484771

LIST OF TABLES

Table 1 - Raingauge index and exact locations as illustrated in Figure 1. Two rain gauges highlighted in bold font are installed at Purchase Knob, a supersite in the inner mountain region. Locations equipped with more than one raingauge (collocated) are shaded in grey color, and these collocated raingauges generally differ in tipping sizes. This table is adapted from Liao and Barros (2019).

Table 2 - Hydrologic skills used in this work.

Table 3 - Information table for selected basins and corresponding streamflow gauges used in this work. This table is adapted from Liao and Barros (2025b). Basin 07 and Basin 12 are the smallest and largest basins respectively and were removed from further analysis. Red-coded rows represent basins located in Karst terrain, which are not included in the final published data due to the lack of Karst hydrology processes in the hydrology model and consequently lesser performance of the IRC.

Table 1 – Raingauge index and exact locations as illustrated in Figure 1. Two rain gauges highlighted in bold font are installed at Purchase Knob, a supersite in the inner mountain region. Locations equipped with more than one raingauge (collocated) are shaded in grey color, and these collocated raingauges generally differ in tipping sizes. This table is adapted from Liao and Barros (2019).

NO.	Site ID.	Latitude	Longitude	Elevation (m)
01	RG 001	35.398	-82.913	1156
02	RG 002	35.417	-82.971	1731
03	RG 003	35.384	-82.916	1609
04	RG 004	35.368	-82.990	1922
05	RG 005	35.408	-82.964	1520
06	RG 008	35.382	-82.973	1737
07	RG 010	35.456	-82.946	1478
08	RG 100	35.586	-83.072	1495
09	RG 100T	35.587	-83.064	1485
10	RG 101	35.575	-83.088	1520
11	RG 102	35.563	-83.103	1635
12	RG 103	35.553	-83.117	1688
13	RG 104	35.554	-83.088	1584
14	RG 106	35.432	-83.029	1210
15	RG 109	35.495	-83.040	1500
16	RG 110	35.548	-83.148	1563
17	RG 300	35.726	-83.216	1558
18	RG 301	35.705	-83.255	2003
19	RG 302	35.721	-83.246	1860
20	**RG 303PK**	**35.586**	**-83.072**	**1495**
21	**RG 303S**	**35.762**	**-83.162**	**1490**
22	RG 304	35.670	-83.182	1820
23	RG 305	35.691	-83.131	1630
24	RG 306	35.745	-83.171	1536
25	RG 307	35.651	-83.199	1624
26	RG 308	35.730	-83.182	1471
27	RG 309	35.682	-83.150	1604
28	RG 310	35.702	-83.122	1756
29	RG 311	35.765	-83.140	1036
30	RG 400	35.702	-83.122	1756
31	RG 401	35.651	-83.199	1624
32	RG 402	35.721	-83.246	1860
33	RG 403	35.517	-83.101	925
34	RG 407	35.517	-83.101	925

Table 2: Hydrologic skills used in this work.

Notation	Information	Reference
KGE	Kling-Gupta efficiency	Eq. (19) /Gupta et al. (2009)
EV	Relative error in flood volume	Eq. (20)
EPT	Error in peak flow timing	Flood front timing differences
EPV	Relative Error in maximum flow rate	Eq. (21)

Table 3 – Information table for initially selected basins and corresponding streamflow gauges used in this work. This table is adapted from Liao and Barros (2025b). Basin 07 and Basin 12 are the smallest and largest basins and were removed from further analysis. Red-coded rows represent basins located in Karst terrain, which were discarded from the final published data due to the lack of Karst analysis in this work.

Basin index	USGS Gauge ID	Drainage area (km^2)	Basin highest elevation (m)	Basin relief (m)	Location
1	3544970	118.7	1442	847	GA
2	2178400	176.1	1629	1051	GA
3	3504000	149.9	1667	1032	NC
4	3497300	317.6	1999	1651	TN
5	3460000	148.1	1879	1174	NC
6	3456500	152.8	1873	1157	NC
7	**3450000**	**15.8**	**1934**	**1047**	**NC**
8	344894205	41.3	1995	1221	NC
9	3463300	134.3	1989	1425	NC
10	3400500	234.7	1257	1257	KY
11	3479000	283.3	1772	1216	NC
12	**3161000**	**611.8**	**1834**	**1009**	**NC**
13	3182700	447.3	1111	717	WV
14	2011460	194.4	1388	763	VA
15	1620500	54.5	1321	712	VA
16	3180500	426.8	1416	621	WV
17	3068800	437.1	1471	908	WV
18	1595000	234.8	1230	560	MD
19	1595300	130.3	1069	712	WV
20	1544500	445.9	765	457	PA
21	1422747	81.4	766	394	NY
22	1415000	106.8	1019	636	NY
23	1413398	152.8	1094	754	NY
24	13621955	41.7	1074	717	NY
25	1421610	51.3	970	497	NY
26	1074520	389.4	1582	1582	NH
27	10642505	294.9	1895	1693	NH
28	1137500	300.3	1894	1546	NH
29	1133000	183.2	975	719	VT
30	1055000	334.1	1143	975	MAINE

LIST OF FIGURES

Figure 1 - Map of IPHEx (Barros et al., 2014) ground-based observations in the Southern Appalachians. Raingauge is denoted as a character string starting with three-digit number potentially followed by extra letters; locations started with a letter P represent disdrometers. The basic information regarding these stations is listed in Table 1. This figure is adapted from Liao and Barros (2019).

Figure 2 – Workflow to generate the product $\mathrm{STIV_{DBKC}}$.

Figure 3 – An illustration of the structure of IRC, ICC and the coupled IRC-ICC framework including **a)** the residual hydrograph between the observed and simulated discharge, with the discharge water difference *wd(t)* being distributed across the time window T; **b)** Example of travel time distribution TT(t) and map (inset) illustrating a hypothetical distribution of runoff source areas (in red, ns=3) with travel time x_2 contributing to streamflow at time t, meaning that at time t-x_2 there are three pixels (ns=3) generating runoff that reaches the outlet at time t. T is the time window over which runoff source areas with TT < T are mapped and the inverse rainfall correction (IRC) are applied; **c)** Example of IRC windows guided by timescales of dominant hydrological processes. The first window solely covers the initial streamflow conditions before the target event. The second window depicts the early rising limb of the hydrograph. The third window captures the steep rising limb of the hydrograph until it reaches the peak flow. The fourth and fifth windows correspond to interflow-dominant and baseflow-dominant stages of the recession curve respectively, separated by the recession inflection point; **d)** A schematic drawing that shows different characteristic timings in a hydrograph with the implementation of the Initial Condition Correction (ICC) strategy. Specifically, T_{r*} and T_r represent the timing of flood front in simulations and observations, respectively. T_p is the timing of observed maximum flood. The inflection point of the recession curve of the observations is denoted as T_I. Flow differences at t_1 and t_2 are denoted as ΔS_1 and ΔS_2 respectively for the purpose of discussion. P, Q and IC represent precipitation, flow discharge and initial condition, respectively; **e)** The implemented framework in this work consisting of ICC and IRC. This figure is adapted from Liao and Barros (2022, 2025b).

Figure 4 – Map of the Continental United States (CONUS) and headwater basins studied in this work. Basin information is available in Table 3. Sub-regions are delineated as the following for discussion purposes only: Northern, Central and Southern Appalachian Mountains (NAM, Basin 21-30; CAM, Basin 13-20; SAM, Basin 01-11). Basins 07 and 12, marked with red symbols, were discarded due to basin size criteria. Basins 13 and 14 with blue symbols were discarded due to the importance of karst hydrology processes that are not represented in the hydrology model used to conduct the IRC. This figure is adapted from Liao and Barros (2025b).

Figure 5 - Examples of raingauge measurements showing the diurnal cycle of different seasons at different locations: Left panel – raingauge RG008 located in the eastern ridges for the Summer (JAS: July-August-September) season. Right panel – raingauge RG302 located in the western ridges for the Spring (AMJ; April-May-June) season. Rain gauge measurements (blue); $\mathrm{StageIV_{DBK}}$ (black); $\mathrm{StageIV_{DBKC}}$ (green). This figure is from Liao and Barros (2019).

Figure 6 –Top row – The diurnal cycle of missing precipitation at RG003 (Eastern ridges) and RG103 (Inner regions) for January-February-March (JFM) using various products. Bottom row-

corresponding rain gauge climatology (blue). StageIV$_{\mathrm{D}}$ (black); StageIV$_{\mathrm{DBK}}$ (cyan); StageIV$_{\mathrm{DBKC}}$ (green). This figure is from Liao and Barros (2019).

Figure 7 – Statistical evaluation summary for winter precipitation (JFM, January, February, and March): a) Diurnal cycle of mean HSS and TS statistics including all rain gauges calculated using all data from 2008 to 2017: STIV$_{\mathrm{D}}$ (black) and STIV$_{\mathrm{DBKC}}$ (green); b) HSS and TS statistics calculated using different rain rate thresholds over the same 10-year period; c) Diurnal cycle of rain rate RMSE at seasonal-scale, and its dependence on observed rainfall rate. This figure is from Liao and Barros (2019).

Figure 8 – The IRC-ICC performance in Basin05 as an example for the 2017-10-23 event (Basin05: Cataloochee Creek Basin, NC). This event is part of the 2017 Hurricane Nate. This figure contains **a)** hydrological responses when precipitation forcing is the STIV$_{\mathrm{DBKC}}$. The dashed rectangular plot consisting of intermediate results including each iteration from the IRC-ICC framework (Figure 3). **b)** the hydrological equilibrium of the IRC-ICC after 5 iterations. This figure is adapted from Liao and Barros (2025b).

Figure 9 – The IRC-ICC performance for different subregions, include **a)** 3 events from the Southern Appalachians; **b)** 3 events from the Central Appalachians; and **c)** 3 events from the Northern Appalachians. The IRC-ICC KGE evolution plots from iterations are included below the hydrographs. The black and pink line are from the original STIV$_{\mathrm{D}}$ and the IRC-ICC equilibrium state ($\mathrm{STIV}_{\mathrm{D}}^{\mathrm{IRC*}}$), respectively, and KGE values are displayed as colored numbers in the top left corners. This figure is adapted from Liao and Barros (2025b).

Figure 10 – Event total precipitation maps for three cold season events (a) and three warm season events (b). Each column represents one event, and each row represents one precipitation product: STIV$_{\mathrm{DBKC}}$, $\mathrm{STIV}_{\mathrm{DBKC}}^{\mathrm{IRC*}}$ from IRC-only framework, and $\mathrm{STIV}_{\mathrm{DBKC}}^{\mathrm{IRC*}}$ from the coupled IRC-ICC framework. This figure is adapted from Liao and Barros (2025b).

Figure 11 – Summary charts of precipitation statistics for all event-total precipitation maps. Basin precipitation average and standard deviation for each event are represented by circles and triangles in the top and bottom panel, respectively. Each panel consists of 3 sub-regions by vertical black lines: the Southern Appalachian Mountains, Central Appalachian Mountains, and Northern Appalachian Mountains. The list of events in Basin 05 (with event number ranging from 55 to 108) in the SAM is highlighted by a blue rectangle for further discussion in the text. The average values of all events for both the mean and the standard deviation are calculated and shown in the top right corner. Black color and pink color represent pre and post IRC-ICC QPE statistics, respectively.

Figure 12 – Summary of hydrologic skills. Green dashed lines and associated uncertainty envelopes are only for visual illustration. Hydrologic statistics are explained in Table 2. Pink and black scatters (each scatter represent one event) represent IRC-ICC, and baseline outputs, respectively. Each horizontal panel is split into 3 subsections by vertical black lines representing the 3 subregions. Histograms graphs on the right hand side are provided for a summary view. This figure is adapted from Liao and Barros (2025b).

Figure 13 – **a**) Event total QPE plots for various QPE datasets conditional on seasons and KGE values; **b**) KGE distributions across events using different QPE datasets. This figure is adapted from Liao and Barros (2025b).

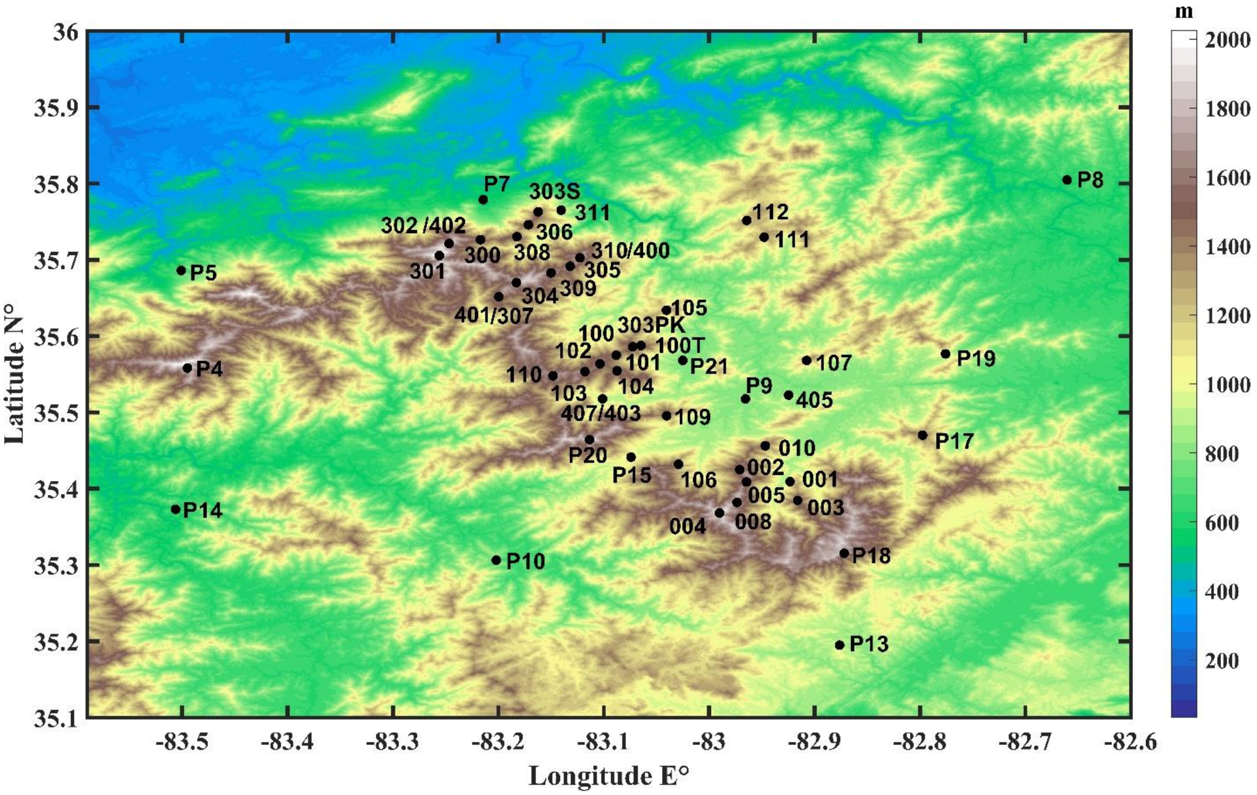

Figure 1 - Map of IPHEx (Barros et al., 2014) ground-based observations in the Southern Appalachians. Raingauge is denoted as a character string starting with three-digit number potentially followed by extra letters; locations started with a letter P represent disdrometers. The basic information regarding these stations is listed in Table 1. This figure is adapted from Liao and Barros (2019).

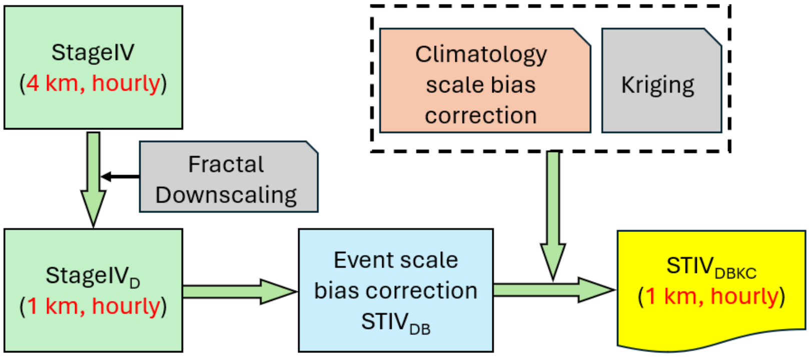

Figure 2 – Workflow to generate the product STIV$_{\mathrm{DBKC}}$.

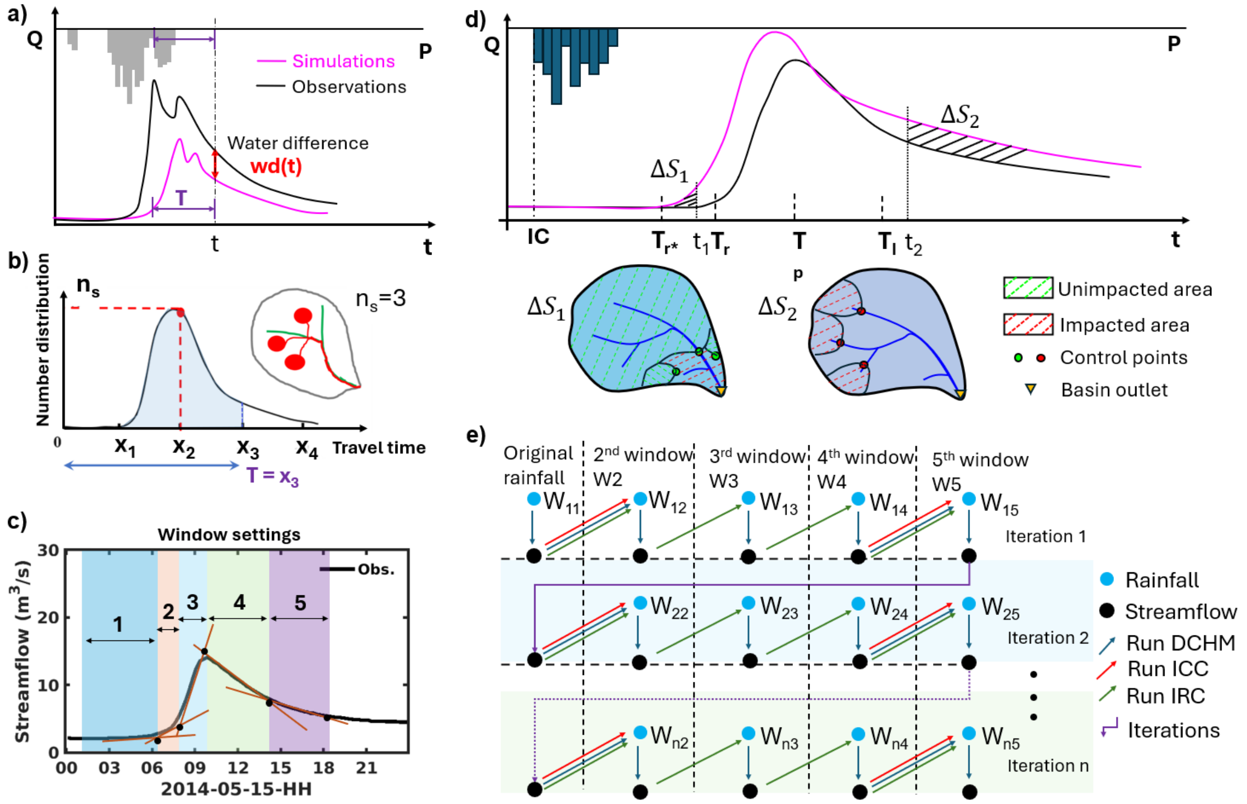

Figure 3 – An illustration of the structure of IRC, ICC and the coupled IRC-ICC framework including **a)** the residual hydrograph between the observed and simulated discharge, with the discharge water difference *wd(t)* being distributed across the time window T; **b)** Example of travel time distribution TT(t) and map (inset) illustrating a hypothetical distribution of runoff source areas (in red, ns=3) with travel time x_2 contributing to streamflow at time t, meaning that at time t-x_2 there are three pixels (ns=3) generating runoff that reaches the outlet at time t. T is the time window over which runoff source areas with TT < T are mapped and the inverse rainfall correction (IRC) are applied; **c)** Example of IRC windows guided by timescales of dominant hydrological processes. The first window solely covers the initial streamflow conditions before the target event. The second window depicts the early rising limb of the hydrograph. The third window captures the steep rising limb of the hydrograph until it reaches the peak flow. The fourth and fifth windows correspond to interflow-dominant and baseflow-dominant stages of the recession curve respectively, separated by the recession inflection point; **d)** A schematic drawing that shows different characteristic timings in a hydrograph with the implementation of the Initial Condition Correction (ICC) strategy. Specifically, T_{r*} and T_r represent the timing of flood front in simulations and observations, respectively. T_p is the timing of observed maximum flood. The inflection point of the recession curve of the observations is denoted as T_I. Flow differences at t_1 and t_2 are denoted as ΔS_1 and ΔS_2 respectively for the purpose of discussion. P, Q and IC represent precipitation, flow discharge and initial condition, respectively; **e)** The implemented framework in this work consisting of ICC and IRC. This figure is adapted from Liao and Barros (2022, 2025b).

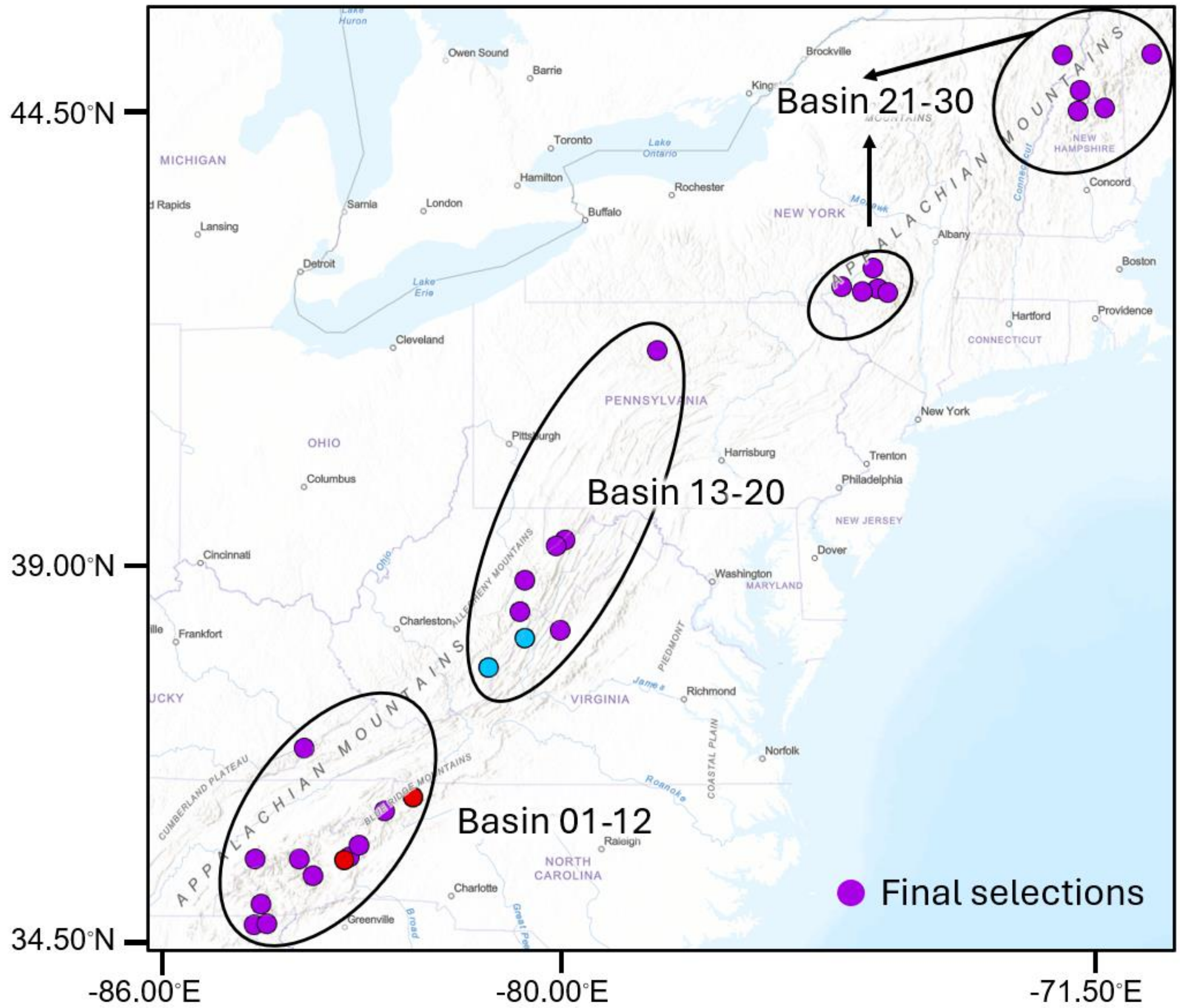

Figure 4 – Map of the Continental United States (CONUS) and headwater basins studied in this work. Basin information is available in Table 3. Sub-regions are delineated as the following for discussion purposes only: Northern, Central and Southern Appalachian Mountains (NAM, Basin 21-30; CAM, Basin 13-20; SAM, Basin 01-11). Basins 07 and 12, marked with red symbols, were discarded due to basin size criteria. Basins 13 and 14 with blue symbols were discarded due to the importance of karst hydrology processes that are not represented in the hydrology model used to conduct the IRC. This figure is adapted from Liao and Barros (2025b).

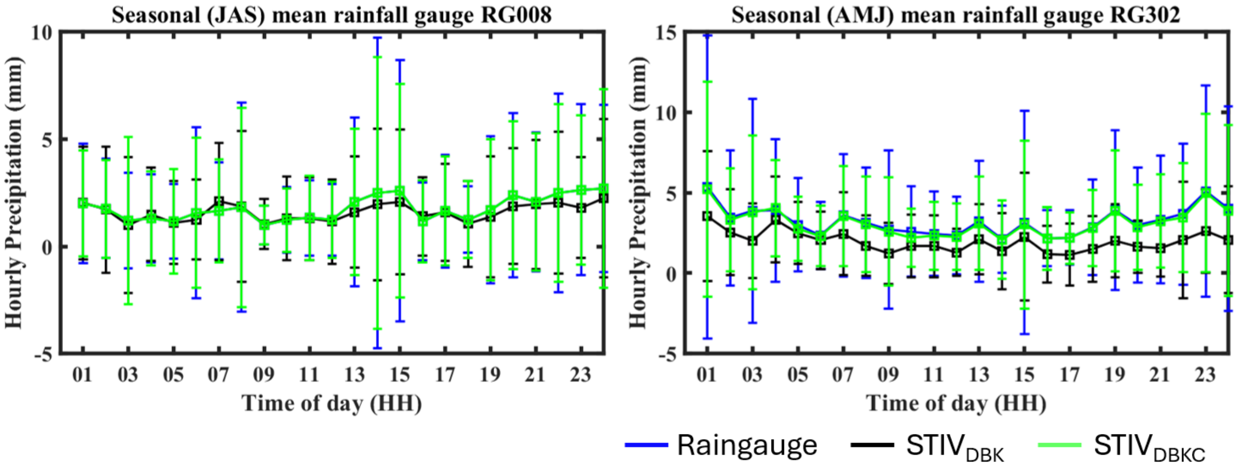

Figure 5 – Examples of raingauge measurements showing the diurnal cycle of different seasons at different locations: Left panel – raingauge RG008 located in the eastern ridges for the Summer (JAS: July-August-September) season. Right panel – raingauge RG302 located in the western ridges for the Spring (AMJ; April-May-June) season. Rain gauge measurements (blue); StageIV$_{DBK}$ (black); StageIV$_{DBKC}$ (green). This figure is from Liao and Barros (2019).

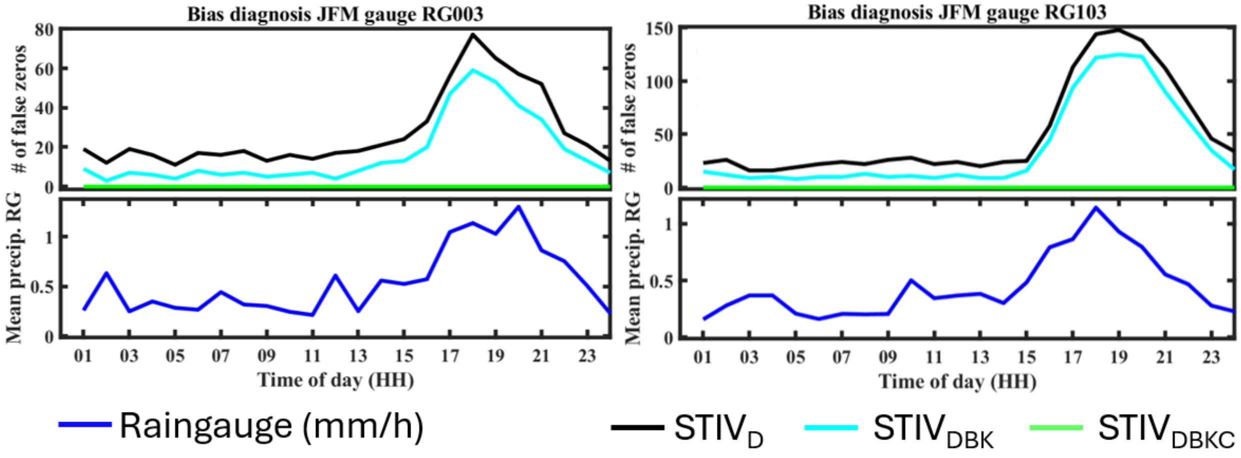

Figure 6 –Top row – The diurnal cycle of missing precipitation at RG003 (Eastern ridges) and RG103 (Inner regions) for January-February-March (JFM) using various products. Bottom row- corresponding rain gauge climatology (blue). $\text{StageIV}_{\text{D}}$ (black); $\text{StageIV}_{\text{DBK}}$ (cyan); $\text{StageIV}_{\text{DBKC}}$ (green). This figure is from Liao and Barros (2019).

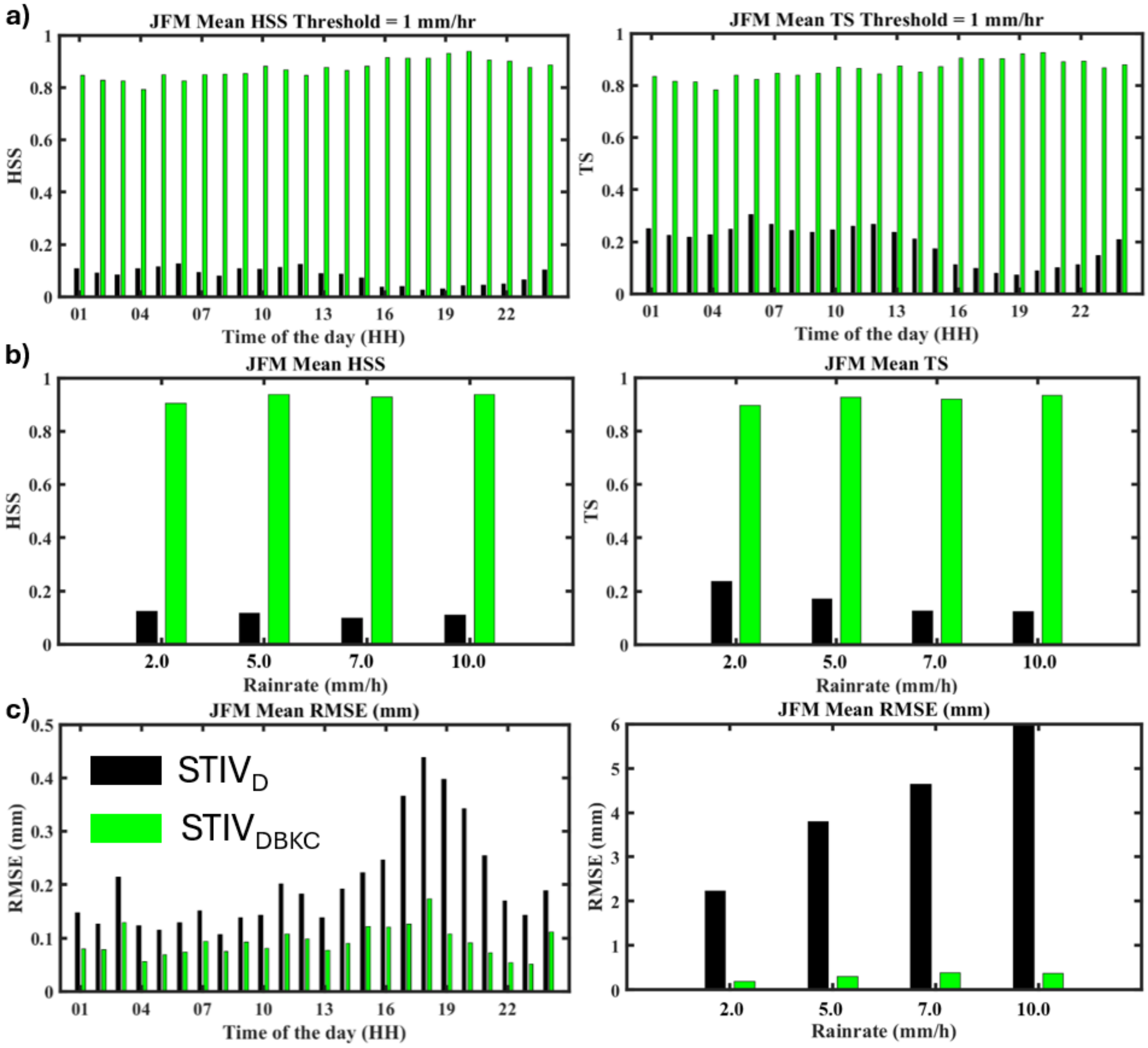

Figure 7 – Statistical evaluation summary for winter precipitation (JFM, January, February, and March): a) Diurnal cycle of mean HSS and TS statistics including all rain gauges calculated using all data from 2008 to 2017: STIV$_D$ (black) and STIV$_{DBKC}$ (green); b) HSS and TS statistics calculated using different rain rate thresholds over the same 10-year period; c) Diurnal cycle of rain rate RMSE at seasonal-scale, and its dependence on observed rainfall rate. This figure is from Liao and Barros (2019).

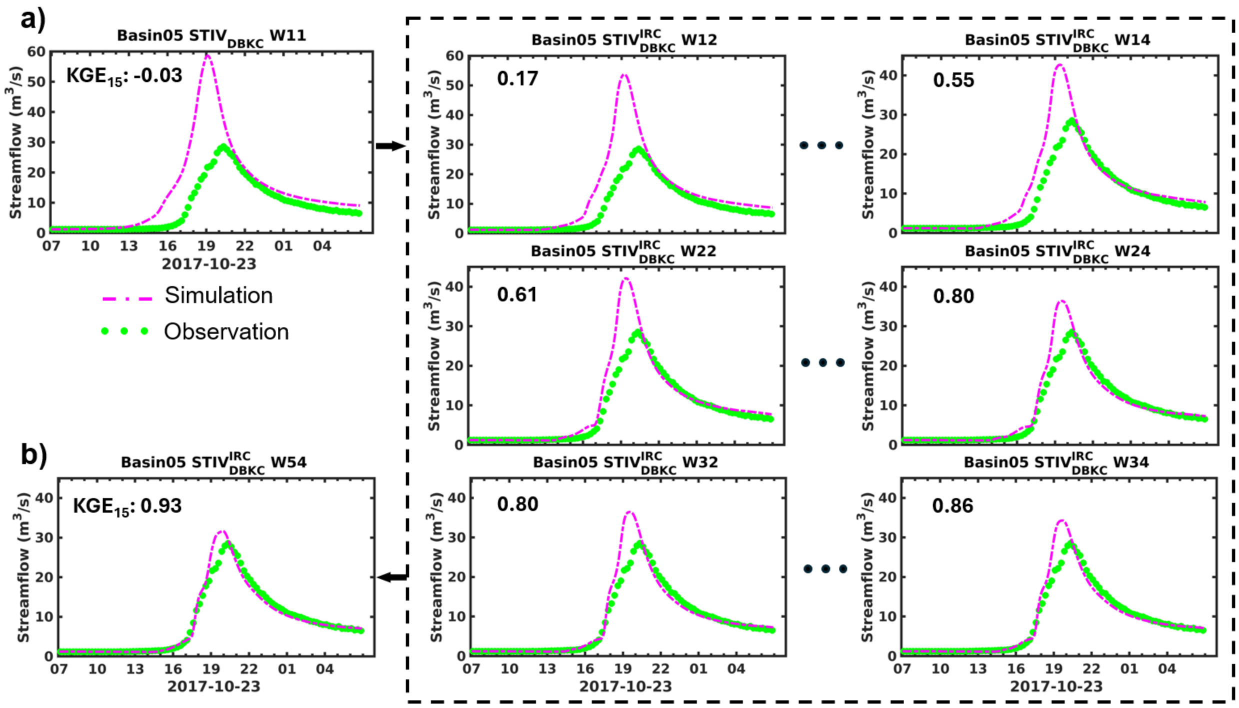

Figure 8 – The IRC-ICC performance in Basin05 as an example for the 2017-10-23 event (Basin05: Cataloochee Creek Basin, NC). This event is part of the 2017 Hurricane Nate. This figure contains **a)** hydrological responses when precipitation forcing is the $\text{STIV}_{\text{DBKC}}$. The dashed rectangular plot consisting of intermediate results including each iteration from the IRC-ICC framework (Figure 3). **b)** the hydrological equilibrium of the IRC-ICC after 5 iterations. This figure is adapted from Liao and Barros (2025b).

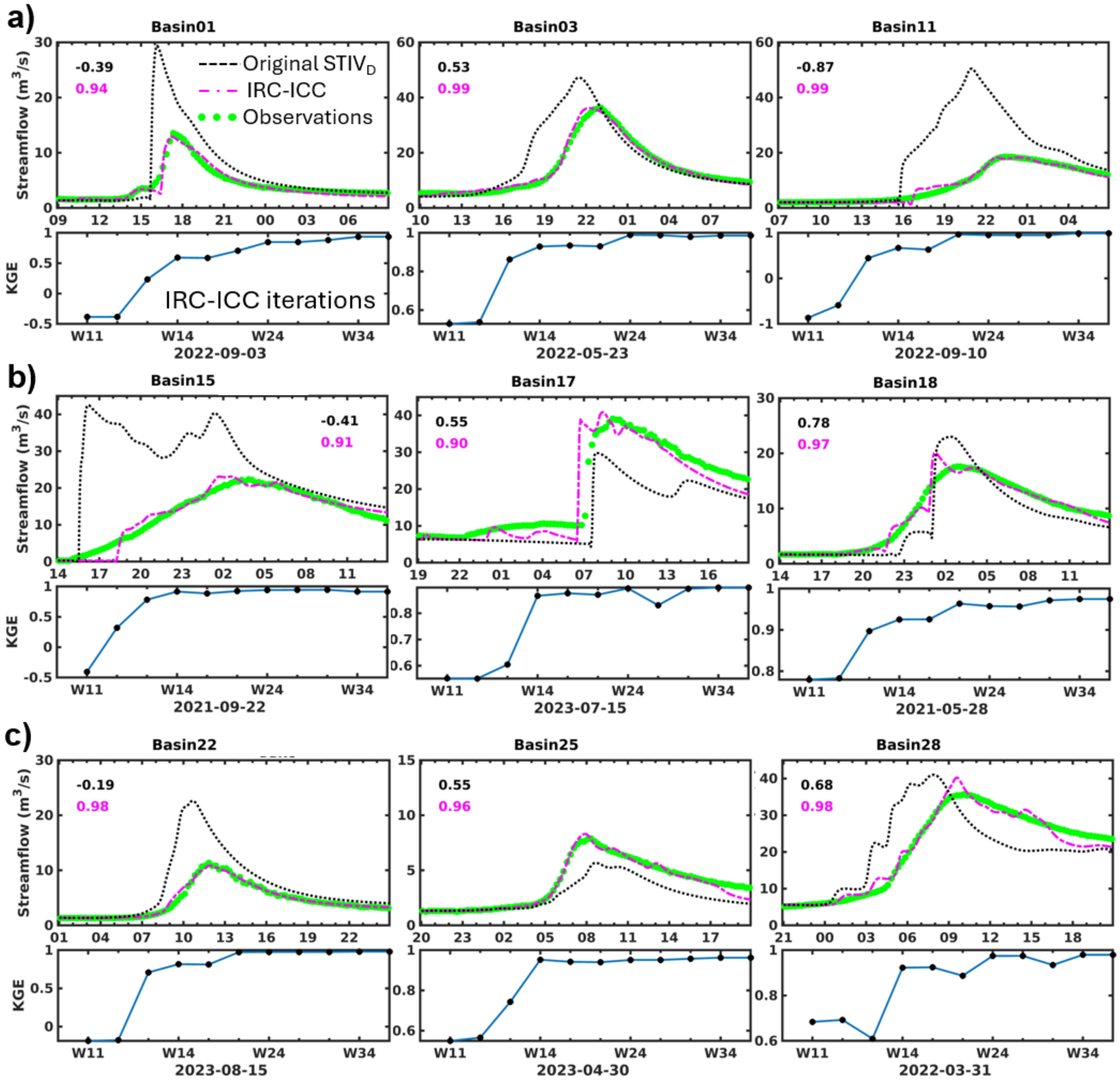

Figure 9 – The IRC-ICC performance for different subregions, include **a)** 3 events from the Southern Appalachians; **b)** 3 events from the Central Appalachians; and **c)** 3 events from the Northern Appalachians. The IRC-ICC KGE evolution plots from iterations are included below the hydrographs. The black and pink line are from the original STIV$_D$ and the IRC-ICC equilibrium state ($STIV_D^{IRC*}$), respectively, and KGE values are displayed as colored numbers in the top left corners. This figure is adapted from Liao and Barros (2025b).

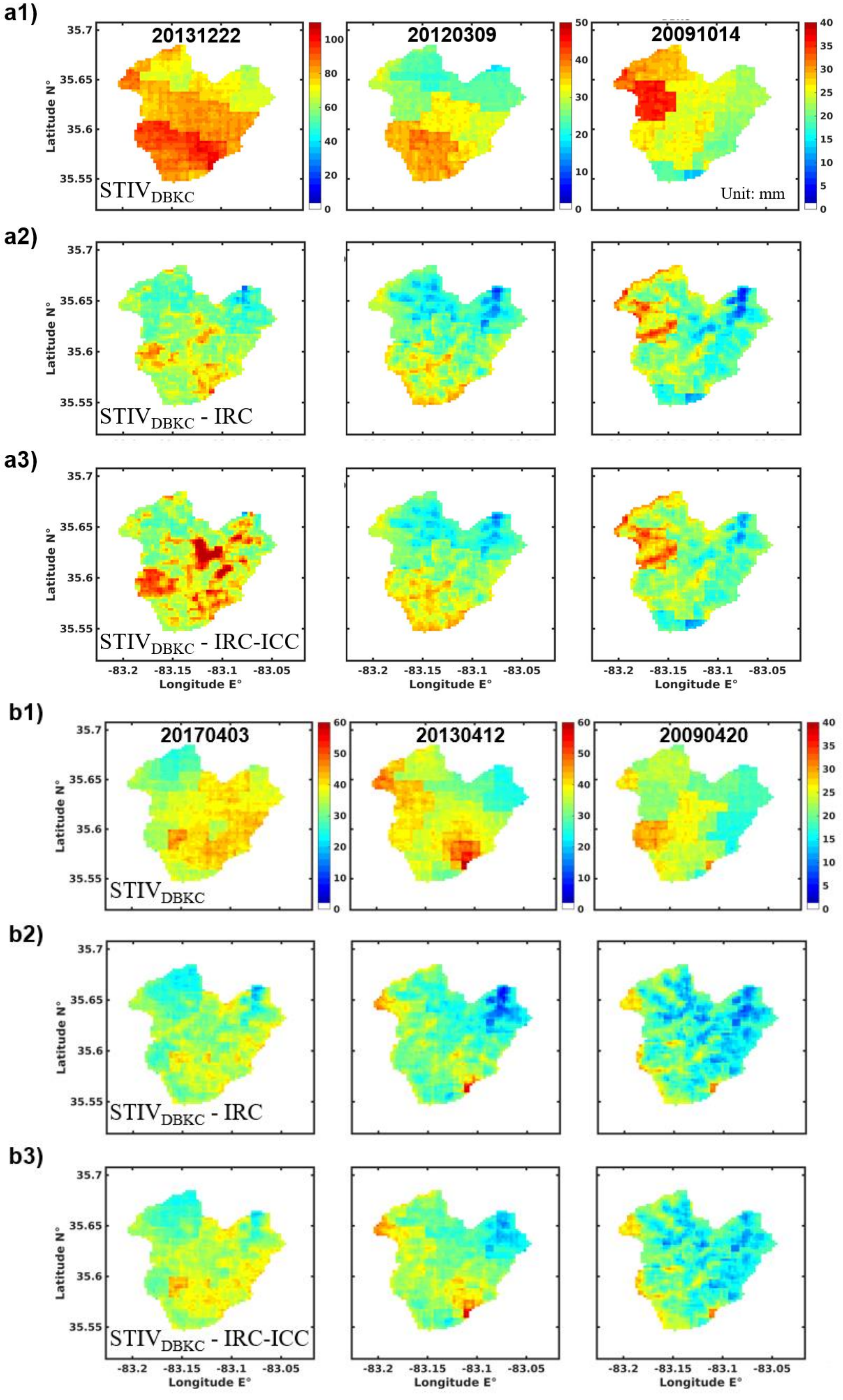
a1)
20131222
20120309
20091014
STIV_DBKC
Unit: mm
a2)
STIV_DBKC - IRC
a3)
STIV_DBKC - IRC-ICC
Latitude N°
Longitude E°
35.55
35.6
35.65
35.7
-83.2
-83.15
-83.1
-83.05
0
20
40
60
80
100
10
30
50
5
15
25
35
b1)
20170403
20130412
20090420
STIV_DBKC
b2)
STIV_DBKC - IRC
b3)
STIV_DBKC - IRC-ICC

Figure 10 – Event total precipitation maps for three cold season events (**a**) and three warm season events (**b**). Each column represents one event, and each row represents one precipitation product: $\mathrm{STIV_{DBKC}}$, $\mathrm{STIV_{DBKC}^{IRC*}}$ from IRC-only framework, and $\mathrm{STIV_{DBKC}^{IRC*}}$ from the coupled IRC-ICC framework. This figure is adapted from Liao and Barros (2025b).

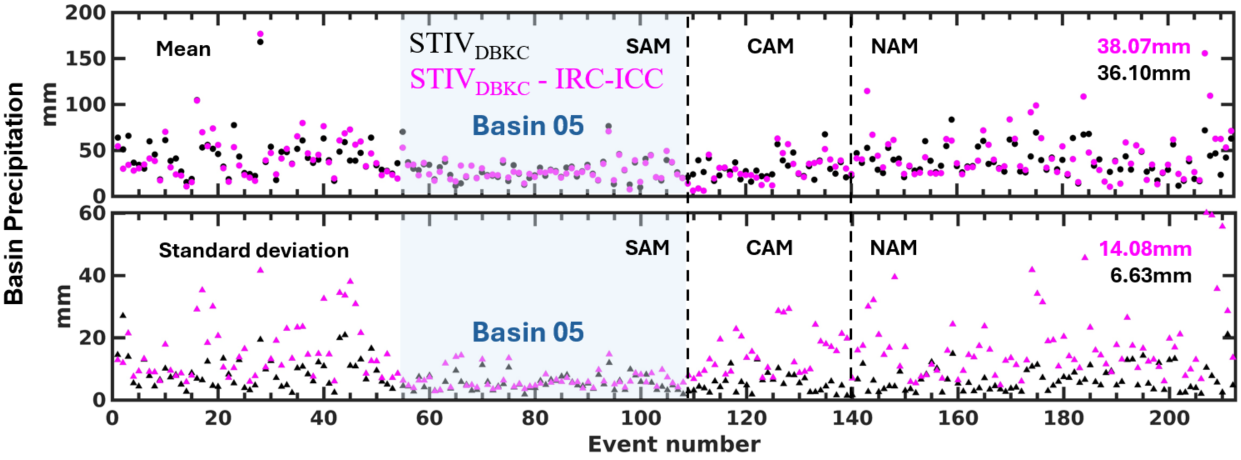

Figure 11 – Summary charts of precipitation statistics for all event-total precipitation maps. Basin precipitation average and standard deviation for each event are represented by circles and triangles in the top and bottom panel, respectively. Each panel consists of 3 sub-regions by vertical black lines: the Southern Appalachian Mountains, Central Appalachian Mountains, and Northern Appalachian Mountains. The list of events in Basin 05 (with event number ranging from 55 to 108) in the SAM is highlighted by a blue rectangle for further discussion in the text. The average values of all events for both the mean and the standard deviation are calculated and shown in the top right corner. Black color and pink color represent pre and post IRC-ICC QPE statistics, respectively.

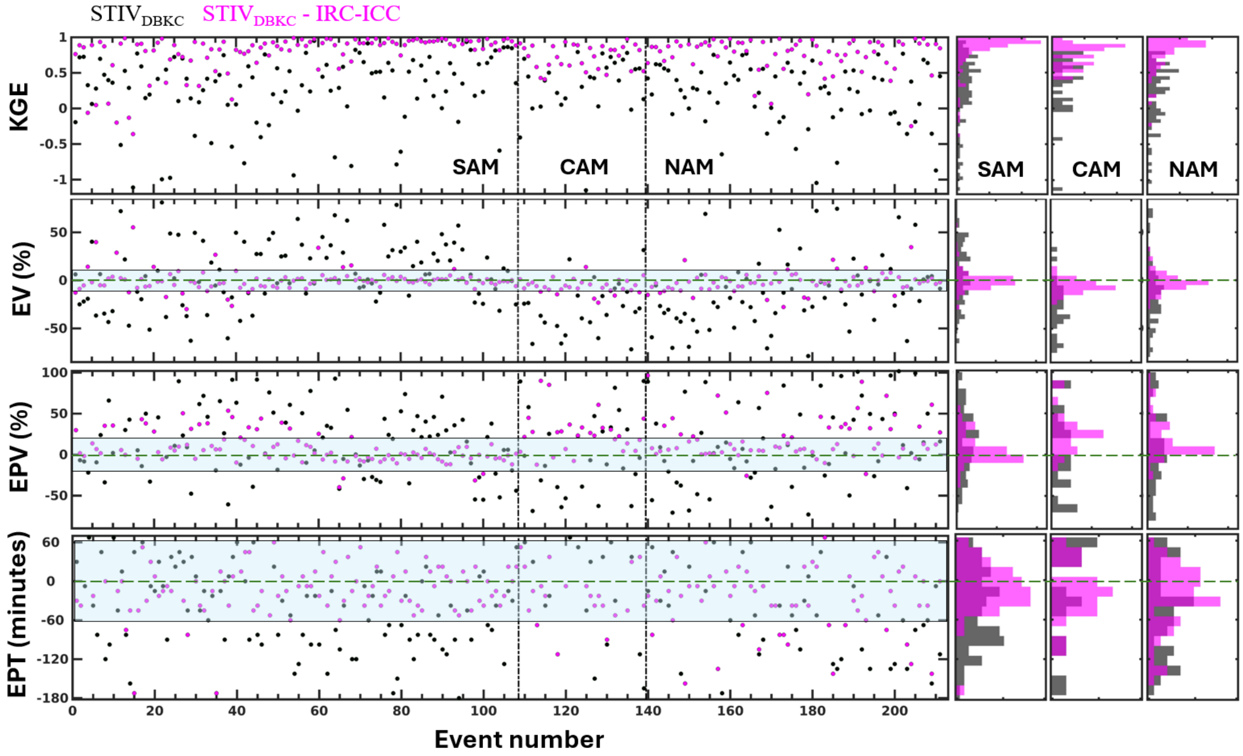

Figure 12 – Summary of hydrologic skills. Green dashed lines and associated uncertainty envelopes are only for visual illustration. Hydrologic statistics are explained in Table 2. Pink and black scatters (each scatter represent one event) represent IRC-ICC, and baseline outputs, respectively. Each horizontal panel is split into 3 subsections by vertical black lines representing the 3 subregions. Histograms graphs on the right hand side are provided for a summary view. This figure is adapted from Liao and Barros (2025b).

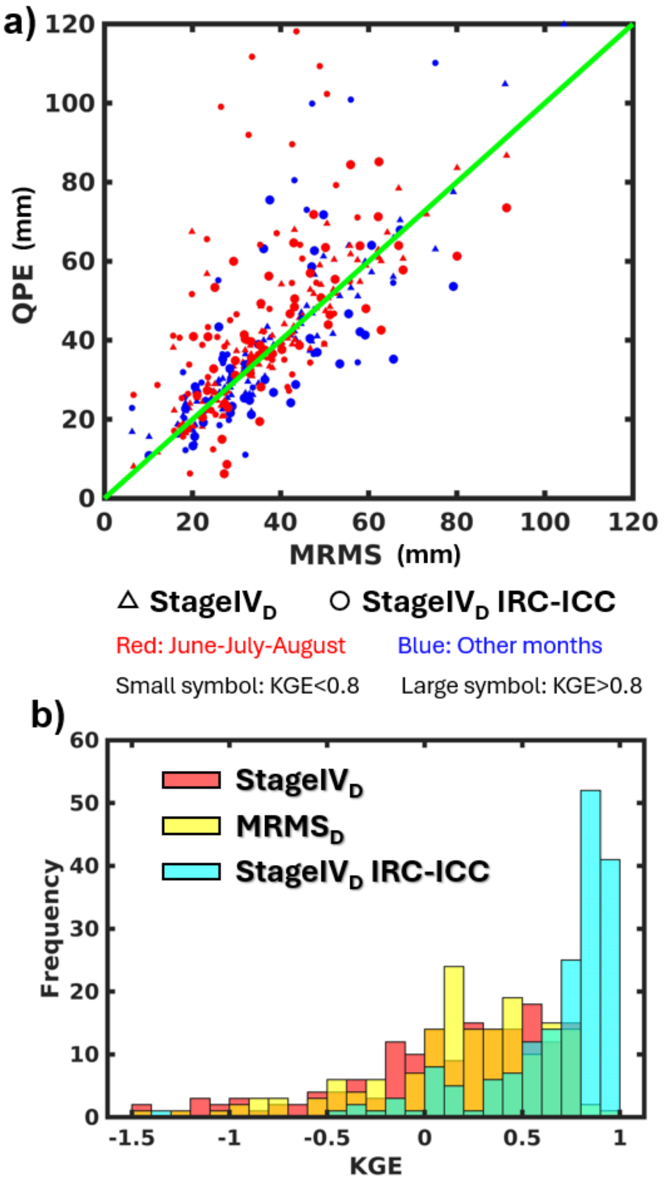

Figure 13 – **a**) Event total QPE plots for various QPE datasets conditional on seasons and KGE values; **b**) KGE distributions across events using different QPE datasets. This figure is adapted from Liao and Barros (2025b).